View metadata, citation and similar papers at core.ac.uk

brought to you by CORE

provided by Digital Repository @ Iowa State University

IOWA STATE UNIVERSITY
Digital Repository

Retrospective Theses and Dissertations

Iowa State University Capstones, Theses and Dissertations

1-1-2002

The effects of silver additions on the dielectric and structural properties of barium titanate

Tiffany Allyn Byrne
Iowa State University

Follow this and additional works at: https://lib.dr.iastate.edu/rtd

Recommended Citation

Byrne, Tiffany Allyn, "The effects of silver additions on the dielectric and structural properties of barium titanate" (2002). *Retrospective Theses and Dissertations*. 19805.
https://lib.dr.iastate.edu/rtd/19805

This Thesis is brought to you for free and open access by the Iowa State University Capstones, Theses and Dissertations at Iowa State University Digital Repository. It has been accepted for inclusion in Retrospective Theses and Dissertations by an authorized administrator of Iowa State University Digital Repository. For more information, please contact digirep@iastate.edu.

The effects of silver additions on the dielectric and structural properties of barium titanate

by

Tiffany Allyn Byrne

A thesis submitted to the graduate faculty

in partial fulfillment of the requirements for the degree of

MASTER OF SCIENCE

Major: Materials Science and Engineering

Program of Study Committee:
David Cann, Co-major Professor
Brian Gleeson, Co-major Professor
Dennis Johnson

Iowa State University

Ames, Iowa

2002

Graduate College
Iowa State University

This is to certify that the master's thesis of

Tiffany Allyn Byrne

has met the thesis requirements of Iowa State University

Signatures have been redacted for privacy

For the Major Program

TABLE OF CONTENTS

CHAPTER 1: INTRODUCTION AND BACKGROUND 1
1.0 Introduction 1
1.1 Background 2
1.1.0 Multilayer Ceramic Capacitors 2
1.1.1 Structure and Dielectric Properties of Barium Titanate 4
1.1.2 Effect of Dopants on Barium Titanate 7
1.1.3 Electrode Materials 12

CHAPTER 2: LITERATURE REVIEW 14
2.0 Silver Effects on Barium Titanate 14
2.1 Defect Chemistry of Barium Titanate 16

CHAPTER 3: EXPERIMENTAL PROCEDURE 21
3.0 Materials Preparation 21
3.1 Property Measurements 22
3.1.0 Capacitance Measurements 22
3.1.1 Lattice Parameter Measurements 24
3.1.2 Grain Size Measurements 24

CHAPTER 4: RESULTS 26
4.0 Electronic Properties 26
4.1 Lattice Parameters 30
4.2 Microstructure 33

CHAPTER 5: DISCUSSION 44
5.0 Trend Overview 44
5.1 Silver Solubility 45
5.2 Grain Growth 47
5.3 Dielectric Response 52
5.4 Conclusion 55

APPENDIX A: DIELECTRIC TEMPERATURE SCANS 57

APPENDIX B: XRD SCANS 69

REFERENCES 75

AKNOWLEDGEMENTS 78

CHAPTER 1: INTRODUCTION AND BACKGROUND

1.0 Introduction

Multilayer ceramic capacitors (MLCC) represent a multibillion dollar industry. In 1994 alone, approximately 125 billion MLCCs were produced at a value of $3.5 billion [1]. They can be found in a variety of applications ranging from automobiles and PCs to the space shuttle. As the industry continues to grow, the demand for smaller and smaller MLCCs with a larger capacitance increases. In connection with this growth is the need to understand how the various materials in an MLCC interact with each other.

MLCCs consist of alternating dielectric and electrode layers (Figure 1.1) [2]. Most of the MLCC's fired in air use barium titanate ($BaTiO_3$) as the dielectric material and a Ag/Pd alloy for the electrodes, although alloys of platinum and gold have been used as well [3]. In recent years, MLCCs utilizing base-metal electrodes have gained viability [2]. The capacitance of a MLCC is given by the equation [2]:

$$C = N\frac{\varepsilon_o KA}{t} \qquad (1.1)$$

where N is the number of dielectric layers, A is the electrode surface area, ε_o is the permittivity in a vacuum (8.854×10^{-7} F/m), K is the dielectric constant and t is the thickness of the dielectric layer. From Equation 1.1 it can be seen that an increase in capacitance can be achieved by either reducing the thickness of the dielectric layers or by increasing the total number of layers. Thinner layers also allow for a reduction in capacitor size, which serves to raise the volumetric efficiency. With current processing technology, the thickness of the dielectric layers is limited to around 3 μm although layers as thin as 1 μm have been reported [4]. However, as the layers get thinner the effects of interactions at the metal electrode-

dielectric interface become increasingly significant: decreasing the lifetime of the capacitor and limiting the thickness allowed for the dielectric layer. Considering the large number of MLCCs used in the electronics industry today, the issue of silver interaction with $BaTiO_3$ and its impact on its dielectric properties is of great interest to capacitor manufacturers. The primary aim of this research will be to determine the effects of minute amounts of silver additives on the perovskite crystal structure, the polycrystalline microstructure, and the dielectric properties of $BaTiO_3$. .

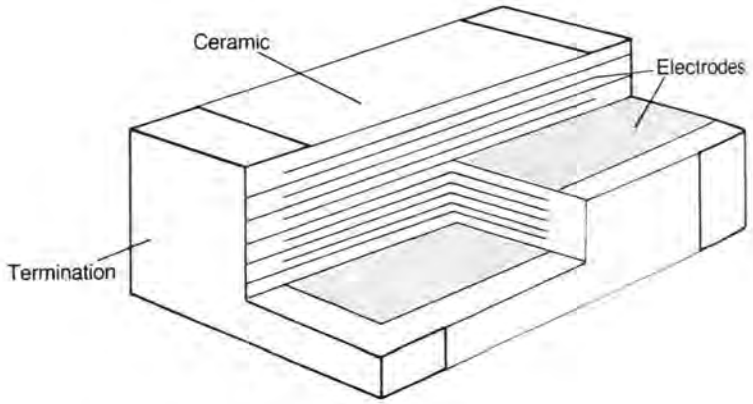

Figure 1.1: Schematic diagram of a multilayer ceramic capacitor (taken from Moulson and Herbert [2])

1.1 Background

1.1.0 Multilayer Ceramic Capacitors

The typical manufacturing process for an MLCC is summarized in Figure 1.2 [5]. First a slip is created from the dielectric powder, which is then tape-cast or wet-screened onto a stable carrier such as a glass plate, stainless steel belt or plastic film. The smallest possible amount of binder is desired in the slip so that shrinkage of the dielectric upon firing is at a minimum thus allowing better control of the final overall dimensions. As soon as the

dielectric layer has reached the preferred thickness, it is dried, and the electrode layer, consisting of a metal ink (metal powder suspended in an organic vehicle), is screen-printed onto the dielectric sheet. These sheets are then stacked and laminated into one piece by applying pressure at temperatures from 40 to 80°C. Several MLCCs are printed onto one large sheet that must be separated into individual devices before firing. The most common method for this operation is razor cutting. The next step in the manufacturing process is binder burnout and co-firing of the MLCC. Firing temperatures range from 900 to 1300°C depending on the powder composition [6]. The final step is the application of the external electrodes. A metal ink consisting of an Ag/Pd metal alloy, glass frit and binder is applied to the exposed internal electrodes. Electrical contacts are then soldered to the terminal electrodes, or if mounted on a circuit board, they are connected directly to the circuit.

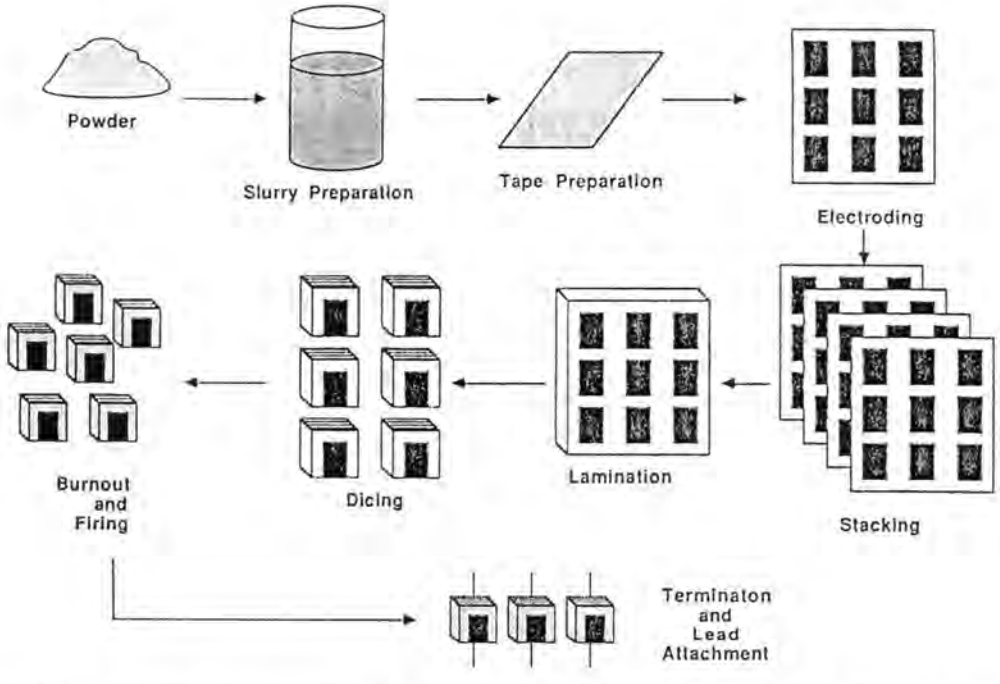

Figure 1.2: Manufacturing process for multilayer ceramic capacitors (taken from Adair, *et al.* [5])

1.1.1 Structure and Dielectric Properties of Barium Titanate

$BaTiO_3$ is one of the most common materials used in multilayer ceramic capacitors because of its large dielectric constant at room temperature (K ~ 2000). This high dielectric constant is due to the ferroelectric nature of the perovskite crystal structure of $BaTiO_3$. As shown in Figure 1.3, the barium atoms are situated at the corners of the unit cell in 12-fold coordination while the titanium atom is located in the center in 6-fold coordination [2]. The oxygen atoms are located in the faces of the unit cell. As can be seen from the phase diagram in Figure 1.4, $BaTiO_3$ is essentially a line compound with little tolerance for both excess BaO and TiO_2 [7-9].

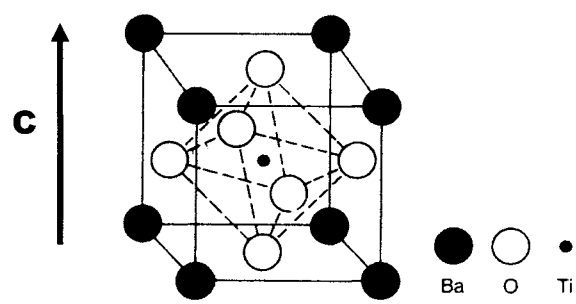

Figure 1.3: Unit cell of $BaTiO_3$ (taken from Moulson and Herbert [2])

Above 130°C, its Curie temperature (T_c), $BaTiO_3$ has a cubic crystal structure (m3m) and is in a paraelectric state. However, below T_c $BaTiO_3$ has a tetragonal crystal structure (4mm) in which the Ba^{2+}, Ti^{4+} and O^{2-} ions are displaced along the **c** axis with the displacement of the O^{2-} ions in an antiparallel direction to the other ions. The result is a spontaneous polarization (P_s) of the material of approximately 20 $\mu C/cm^2$ [2].

In addition to the ferroelectric transition, there are two other phase transitions at lower temperatures. The transition from a tetragonal to orthorhombic structure occurs at 0°C and from orthorhombic to rhombohedral at –90°C. The dielectric constant of $BaTiO_3$ increases at

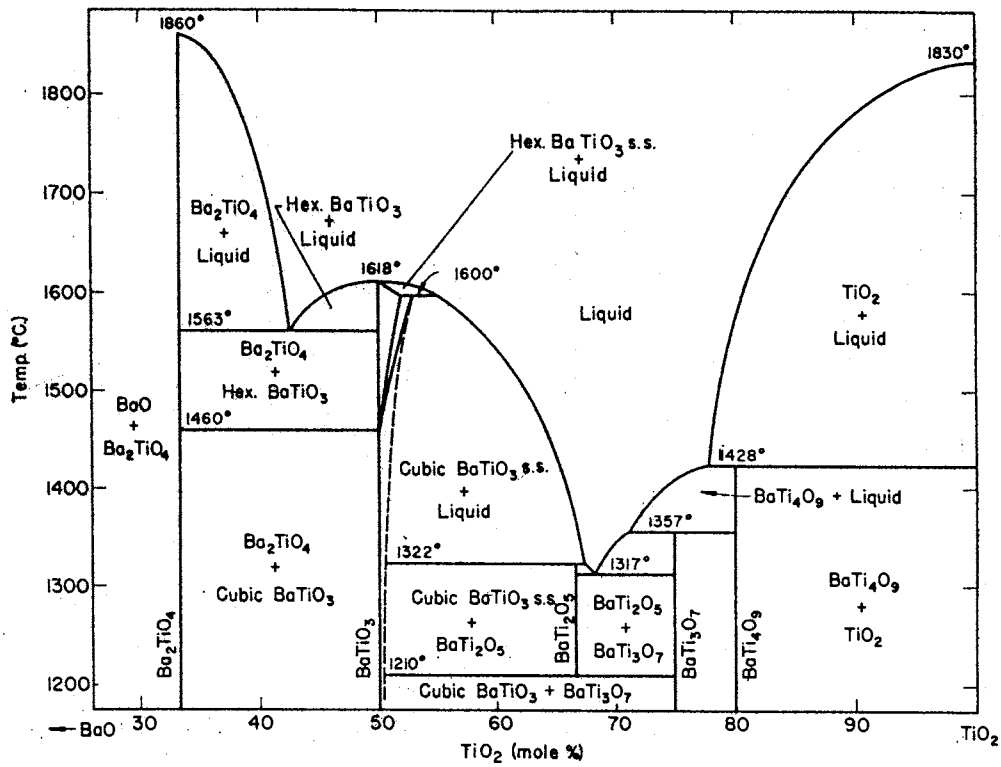

Figure 1.4: Phase equilibrium diagram for the system of BaO-TiO_2 (taken from Rase and Roy [7])

each of these phase transitions but is greatest at the tetragonal-cubic transition temperature (Figure 1.5) [2]. This dramatic increase of K at a phase transition is primarily due to the lattice potential becoming less stable or "softening" allowing the Ti^{4+} ions greater freedom of movement. The result is an enhancement of the amount of polarization that can be experienced by the material [6].

The ferroelectric phase transition is usually a 1st order transition but a 2nd order transition is also possible [10]. The primary distinction between the two types is the temperature dependence of P_s in the vicinity of T_c (Figure 1.6). For 1st order ferroelectrics, there is an instantaneous jump in P_s at T_c caused by a volume change (and hence an enthalpy change). In 2nd order ferroelectrics, P_s increases gradually at T_c. The order of the transition is mainly influenced by the amount of stress experienced by the material and a switch from

one type to another has occurred through a decrease in grain size, doping of the material or application of an external stress.

As seen in Figure 1.5, the dielectric constant is highly temperature dependent. For temperatures above T_c, this behavior can be described by the Curie-Weiss Law [10-13].

$$K = \frac{C}{T - \theta_c} \qquad (1.2)$$

where C is the Curie constant and θ_c the Curie-Weiss temperature, which is close to but below the Curie temperature.

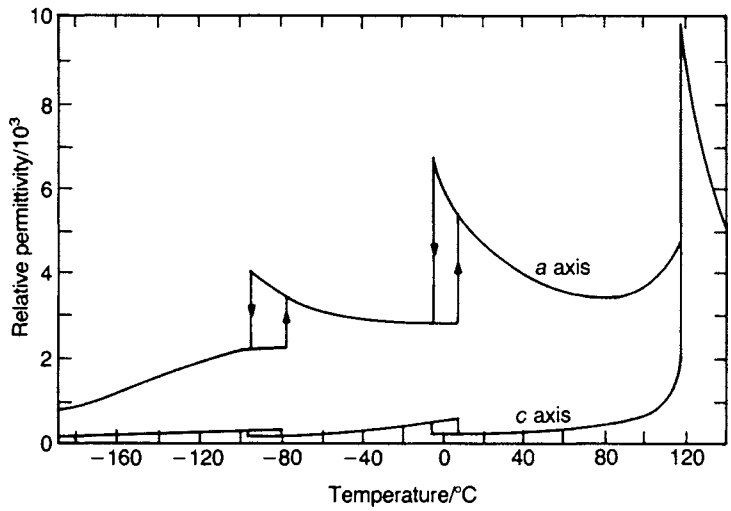

Figure 1.5: Dielectric constant along the **a** and **c** axis as a of function temperature for $BaTiO_3$ (taken from Moulson and Herbert [2])

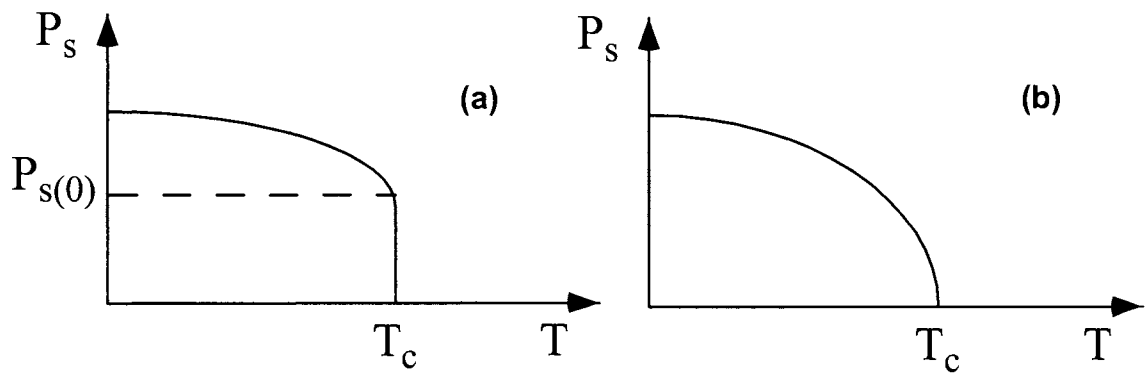

Figure 1.6: Sponstanious polarization as a function of temperature for (a) 1st order transition and a (b) 2nd order transition

1.1.2 Effect of Dopants on Barium Titanate

An attractive aspect of $BaTiO_3$ as a MLCC material is that its dielectric properties can easily be controlled through the doping of ions into the perovskite structure some of which are listed in Table 1.1. Substitution is primarily controlled by the ionic radii of the doping ions, the dopant's valance state and the coordination of the occupation site. According to a study conducted by Roy [14] on the perovskite crystal structure, the A site can accommodate ions ranging roughly from 1.00 to 1.40 Å and the B site from 0.45 to 0.75 Å. Recently it has been discovered that, for certain rare earth elements, the Ba:Ti ratio and the oxygen partial pressure also factor in which site a doping ion occupies [15-19]. When introduced into $BaTiO_3$ dopants, in general, reduce the tetragonality of the perovskite structure (Figure 1.7) [16, 18, 20].

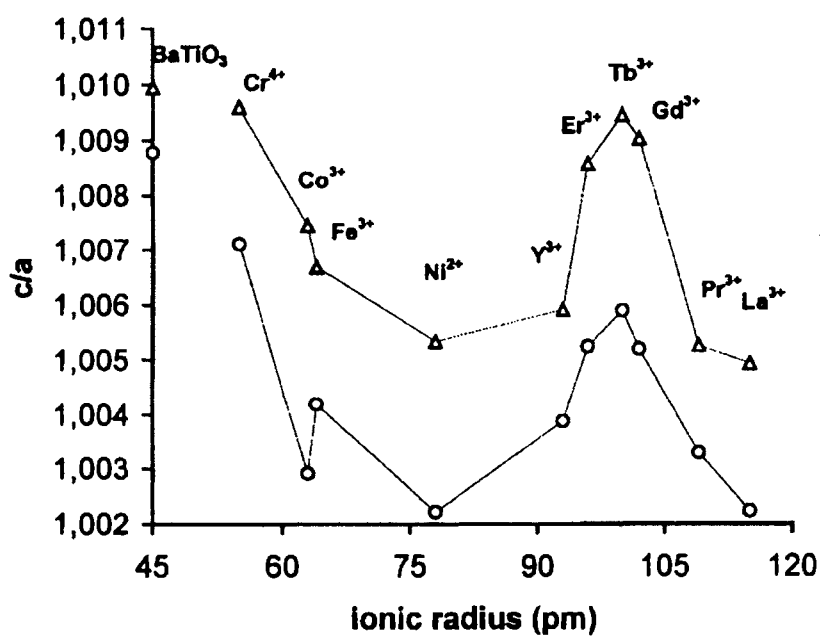

Figure 1.7: The c/a ratio of 1 mol% doped $BaTiO_3$ as a function of dopant ionic radius annealed for 14 hours at 950°C (O) and 1350°C (Δ). The points corresponding to undoped $BaTiO_3$ were placed on the vertical axis as a reference (taken from Buscaglia, *et al.* [16]).

Table 1.1: Common dopants and their applications

Ion	Occupied Site	Ionic Radius† (Å)	Solubility Limit (mol %)	Common Capacitor Applications	Ref.
Pb^{2+}	Ba	1.33 (1.63)	100	shift T_c	2
Sr^{2+}	Ba	1.32 (1.58)	100	shift T_c	2
Ca^{2+}	Ba/Ti*	1.14 (1.48)	Ba: 18 Ti: 2	donor compensation shift T_c	15, 21
Zn^{2+}	Ti	0.88	2	donor compensation	2
Mg^{2+}	Ti*	0.86	-----	donor compensation	2
Ni^{2+}	Ti	0.83	2	control grain growth donor compensation	2, 16, 22
La^{3+}	Ba	1.17 (1.50)	10	reduce resistivity control grain growth improve breakdown resistance	2, 16, 17-19, 23
Pr^{3+}	Ba	1.13 (1.46)	-----	reduce resistivity control grain growth	16
Nd^{3+}	Ba	1.12 (1.41)	5‡	reduce resistivity control grain growth	16, 17, 23
Sm^{3+}	Ba/Ti	1.10 (1.38)	-----	reduce resistivity control grain growth	2, 16, 17, 24
Gd^{3+}	Ba/Ti	1.08 (1.41)	3‡	reduce resistivity	16-18
Dy^{3+}	Ba/Ti	1.05 (1.38)	-----	reduce resistivity control grain growth improve breakdown resistance	2, 16, 23
Y^{3+}	Ba/Ti	1.04	Ba: 1.5 Ti: 12	reduce resistivity improve breakdown resistance	16, 17, 23
Ho^{3+}	Ba/Ti	1.04 (1.37)	-----	reduce resistivity improve breakdown resistance	16, 19, 25
Er^{3+}	Ba/Ti	1.03 (1.36)	-----	reduce resistivity improve breakdown resistance	16, 17
Yb^{3+}	Ti	1.01	6‡	donor compensation, shift T_c	17-19
Ga^{3+}	Ti	0.76	2	donor compensation shift T_c	2
Cr^{3+}	Ti	0.76	2	donor compensation, shift T_c	2, 16
Fe^{3+}	Ti	0.69	1.25	donor compensation, shift T_c	2, 16
Co^{3+}	Ti	0.69	2	donor compensation, shift T_c	2, 16
Zr^{4+}	Ti	0.86	100	control grain growth, shift T_c	2, 22
Sn^{4+}	Ti	0.83	10	control grain growth, shift T_c	20, 26
Mn^{4+}	Ti	0.67	2	donor compensation, reduces tan δ	2
Nb^{5+}	Ti	0.82	5	reduce resistivity control grain growth	16, 27
Sb^{5+}	Ti	0.74	10	reduce resistivity	2, 28

* substitutes on Ti site only if Ba:Ti > 1

† radii in parentheses are for 12-fold coordination, all others for 6-fold coordination [29, 30]

‡ dopant concentration at which $BaTiO_3$ becomes cubic at room temperature

Shifting T_c and reducing the temperature dependence of the dielectric constant are some of the key functions of dopants in $BaTiO_3$. For many capacitor applications it is desirable that T_c be as close to room temperature as possible for optimum performance. In addition, most devices are required to perform over a range of temperatures, and therefore the dielectric constant must remain uniform over this range. There are numerous dopants that have an effect on T_c, but the ones commonly used for this purpose are isovalent ions that form a solid solution with $BaTiO_3$ over a wide range of compositions (Sr, Pb, Zr, Ca, Sn) thus allowing T_c to be tailored for specific applications (Figure 1.8) [2]. The effects of various ions frequently are divided into two categories: shifters and pinchers. Shifter ions like Ca^{2+} and Pb^{2+} displace the entire transition-temperature curve to higher or lower temperatures. Pincher ions like Zr^{4+} and Sn^{4+} shift the tetragonal transition to lower temperatures while raising the orthorhombic and rhombohedral transitions to higher temperatures, thereby "pinching" the transitions together [6].

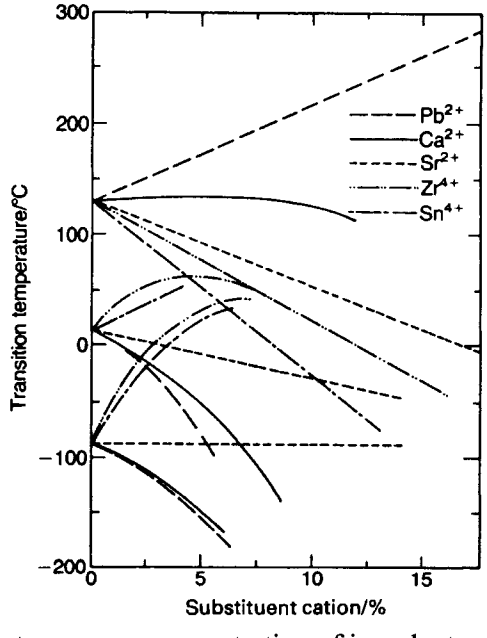

Figure 1.8: Transition temperature versus concentration of isovalent substituents in $BaTiO_3$ (taken from Moulson and Herbert [2])

In order to broaden the temperature range of the high dielectric response, a combination of dopants and liquid phase sintering techniques are used to develop a core-shell microstructure, which, as shown in Figure 1.9, consists of a pure $BaTiO_3$ core surrounded by a highly doped shell [31-37]. Small amounts of flux are added to the $BaTiO_3$ powder to create a liquid phase during firing. As the liquid phase forms, it begins to dissolve the pure $BaTiO_3$ grains. Yet because only a small amount of flux is used, the $BaTiO_3$ grains remain mainly undissolved creating the pure $BaTiO_3$ core. The liquid phase melt quickly becomes saturated with $BaTiO_3$, and the solution-precipitation process begins. During this process, small grains are dissolved due to their higher chemical potential [38]. The melt then reprecipitates epitaxially onto the larger grains, which have a lower chemical potential. Because the melt mainly consists of modifiers, this forms a highly doped shell around the core. As the shell grows, progressively more dopants are incorporated creating a concentration gradient. Limited diffusion of the dopants keeps them trapped with the end result being a ferroelectric core encircled by a non-ferroelectric shell [32, 38]. The final dielectric-temperature behavior then becomes the sum of the core and shell profiles resulting in a relatively temperature independent dielectric response.

Besides controlling T_c, dopants can be used to modify the electronic properties of $BaTiO_3$. Less than 0.5 mol% of donor ions like La^{3+} or Nb^{5+} will yield a semiconducting oxide used for positive coefficient of resistivity (PTCR) applications. However, at higher dopant concentrations the insulating properties are restored with an improved resistance to dielectric breakdown due to a combination of grain size reduction and compensation of oxygen vacancies [2, 16]. Many rare-earth elements are also added to enhance degradation

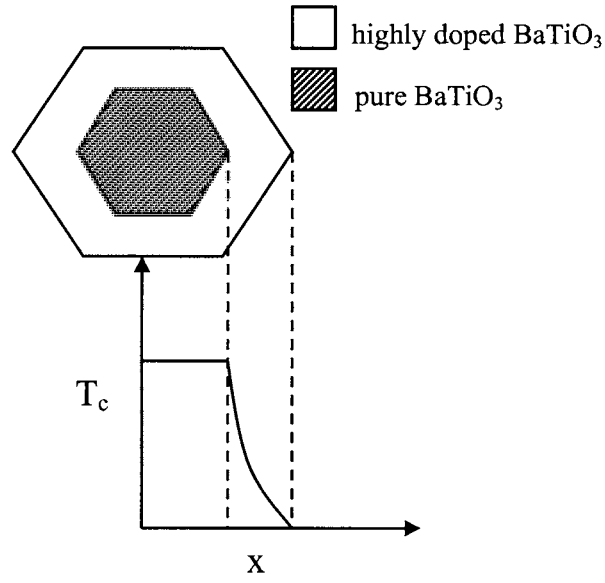

Figure 1.9: Schematic of core-shell structure in $BaTiO_3$ detailing the Curie temperature as a function of distance through the grain

resistance in MLCCs. These dopants are unique in that their behavior is partially determined by the Ba:Ti ratio. For example, Y^{3+} behaves as an acceptor substituting on the Ti site when Ba:Ti > 1 and as a donor substituting on the Ba site when Ba:Ti < 1. When Ba:Ti = 1, Y^{3+} can be found on both sites providing self-compensation [16, 17]. Acceptor ions such as Ca^{2+}, Cr^{3+} and Fe^{3+} are often added to balance electronic charge carriers formed when $BaTiO_3$ is fired under reducing conditions. This has allowed the introduction of base-metal electrodes (i.e. Ni) to MLCC manufacture. Another frequent addition is Mn^{4+} due to its effectiveness in reducing the dissipation factor [2].

Finally, dopants are used to control the grain size, which has a substantial effect on the dielectric constant of $BaTiO_3$. As the grain size decreases, the dielectric constant increases (Figure 1.10) due to a rise in the number of 90° domains [39, 40]. When the grains are large, the residual stress caused by the transition from the cubic to tetragonal phase is relieved by the formation of both 90° and 180° ferroelectric domains. However, as the grain

size approaches 1 μm, fewer domains can be formed in each grain and the 180° domains disappear. Below 1 μm, the dielectric constant again decreases. A number of theories have been proposed to explain this phenomenon. One states that the high stress experienced in fine grain structures forces $BaTiO_3$ to remain in a "pseudocubic" phase [40]. Another theory put forward by Frey, *et al.* [39] asserts that the dilution effect of the low K grain boundaries becomes an increasingly important factor. In general, small grains are desired and many dopants (La, Nb, Zr, Dy, Mg) are added to inhibit grain growth.

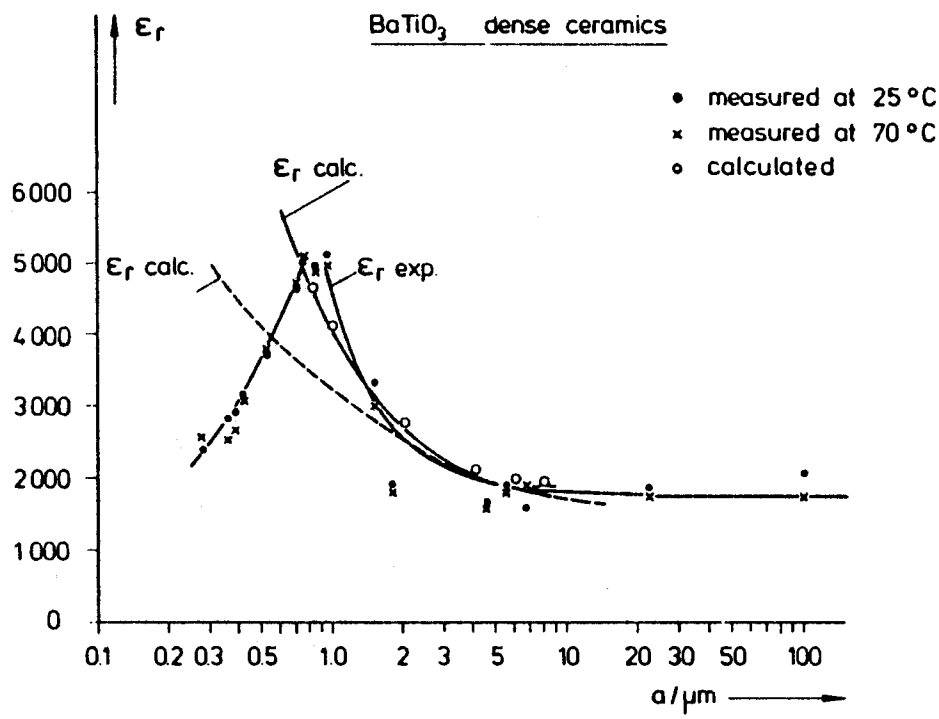

Figure 1.10: The effect of grain size on the dielectric constant of $BaTiO_3$ (taken from Arlt, Hennings and de With [40])

1.1.3 Electrode Materials

Because the electrodes are responsible for the bulk of the overall cost (30–60%) of manufacturing MLCCs, there is a great drive to reduce the amount of noble metals used in the internal electrodes [6]. Most electrodes are made of an Ag/Pd alloy, which creates a solid

solution over a large temperature range. As can be seen in the phase diagram in Figure 1.11, the higher the firing temperature the larger the amount of palladium needed in order to keep the electrodes from melting during cofiring of the MLCC with the most common compositions being a 70Ag/30Pd alloy for low fire dielectrics and 30Ag/70Pd for high fire. Typically additives are required to lower the sintering temperature of the $BaTiO_3$ to allow for electrode compositions with lower palladium content to be used. Fluxes consisting of Bi_2O_3, PbO, ZnO and B_2O_3 are commonly used for ultra low fire powders (sintering temperature ~ 900°C) [1, 37].

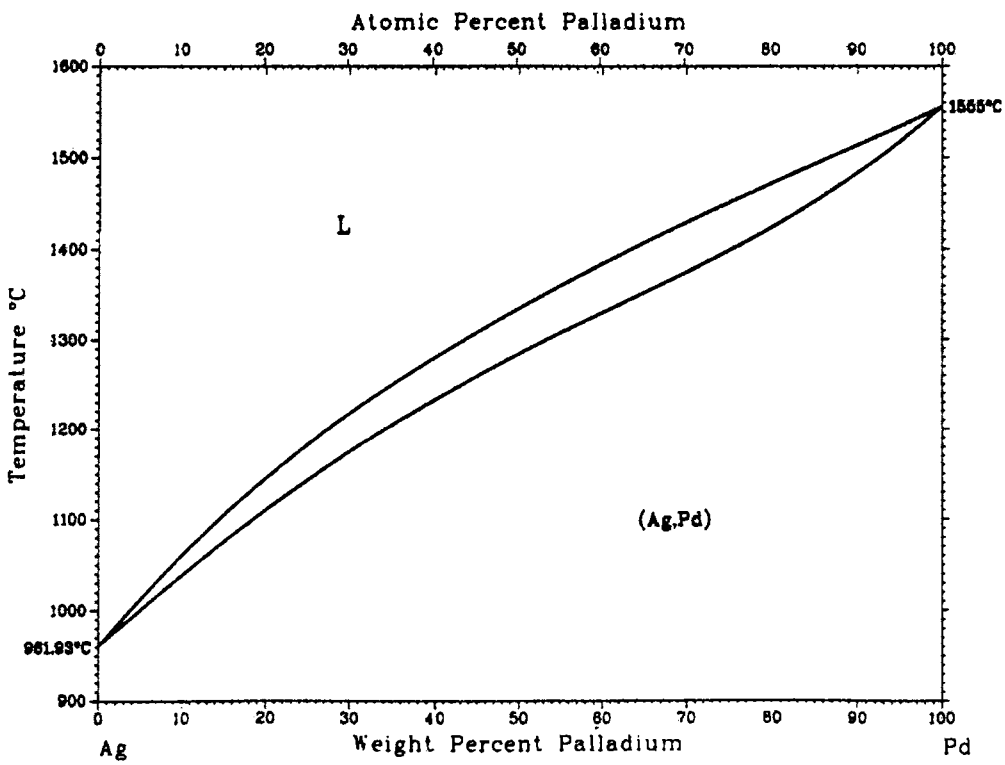

Figure 1.11: Phase diagram for Ag-Pd system (taken from *Binary Alloy Phase Diagrams* [41])

CHAPTER 2: LITERATURE REVIEW

2.0 Silver Effects on Barium Titanate

The effect of silver on the sintering and dielectric behavior has not been investigated extensively. However, some studies have been conducted, most notably those of Chen and Tuan [42, 43]. They observed that small amounts of silver promoted the growth of abnormal grains, serving as starting points for heterogeneous nucleation. This behavior reaches its peak at 0.3 wt% Ag as seen in Figure 2.1. Above 0.3 wt%, the increasing size and number of silver inclusions impedes the grain growth process. Similar effects have been noted in lead zirconate-titanate (PZT) [44]. Measurements of the dielectric constant showed a marked decrease due to the grain size effect. On the other hand, no change was observed in the lattice parameters and T_c. The densification rate decreased slightly upon the addition of silver. Also, Chen and Tuan noted that silver migration mainly occurred through vapor phase transport along the open pore structure, another phenomenon observed in PZT [44-51]. From EPMA measurements, the authors determined that the solid solubility of silver in $BaTiO_3$ was less than 300 ppm, the detection limit of their equipment.

An earlier study conducted by Ikushima and Hayakawa [52] observed that silver doped $BaTiO_3$ fired in a nitrogen atmosphere behaved as an n-type semiconductor with the resistivity decreasing with increasing silver content. They also saw no change in the lattice parameters of $BaTiO_3$ but did detect a decrease in T_c with rising silver concentration (Figure 2.2). Another analysis performed by Halder, *et al.* [53] on Z5U $BaTiO_3$ noted that the dielectric constant increased with increasing amounts of silver, peaking at 0.2 wt% Ag. This was attributed to a higher density for the sintered body. Another contribution was credited to

the dispersion of conducting particles in a dielectric matrix, which, in small amounts, would contribute to the dielectric constant by reducing the effective electrode distance. A steady decrease in the dissipation factor (tan δ) was observed as the silver content increased. Measurements of the temperature coefficient of capacitance (TCC) showed no change, however. The observations and conditions of the various studies have been compiled in Table 2.1.

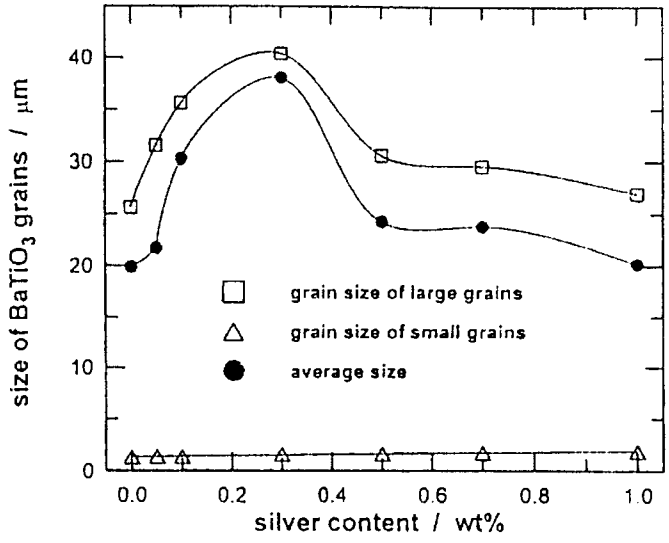

Figure 2.1: Grain size of $BaTiO_3$ as a function of silver content (taken from Chen and Tuan [43])

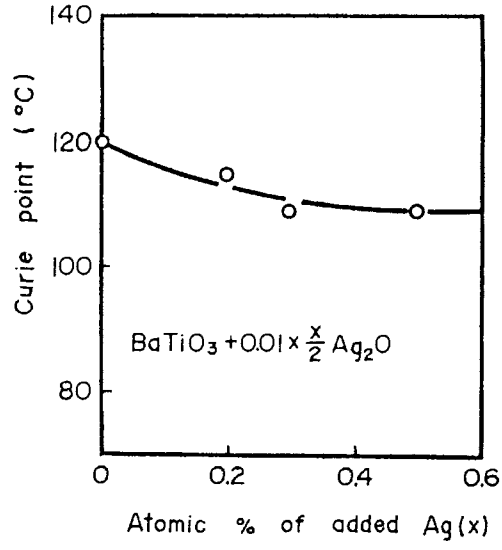

Figure 2.2: Curie point of nitrogen-fired $BaTiO_3$ measured by differential thermal analysis as a function of silver content (taken from Ikushima and Hayakawa [52])

Table 2.1: Summary of studies conducted on the effects of silver on $BaTiO_3$

Author	Material	Sintering Atmosphere	Observations
Chen and Tuan	$BaTiO_3$	air	1. maximum in grain size at 0.3 wt% Ag 2. no change in T_c 3. no change in lattice parameters 4. densification rate decreases 5. K decreases 6. silver migrates by vapor transport through pore channels 7. silver solubility < 300 ppm
Ikushima and Hayakawa	$BaTiO_3$	N_2	1. T_c decreases 2. no change in lattice parameters 3. resistivity decreases
Halder, *et al.*	Z5U $BaTiO_3$	air	1. maximum in K at 0.2 wt% Ag 2. maximum in density at 0.1 wt% Ag 3. no change in the temperature coefficient of capacitance 4. tan δ decreases

2.1 Defect Chemistry of Barium Titanate

The defect chemistry of $BaTiO_3$ is a complex area that has been the subject of a considerable amount of research [54-60]. The primary defects in $BaTiO_3$ consist of barium, titanium and oxygen vacancies. Interstitial defects are energetically unfavorable due to the tight packing of the perovskite structure, and no evidence of them has been found [61]. From the diffusion activation energies of these defects listed in Table 2.2, it can be seen that oxygen vacancies are the most mobile species [62]. The migration of oxygen vacancies is believed to be the cause of insulation resistance degradation in Ni-based MLCCs [63].

Table 2.2: Activation energy of defect diffusion in $BaTiO_3$[62]

Vacancy	Theoretical Activation Energy (eV)	Experimental Activation Energy (eV)
$V_{Ti}^{////}$	15.3	-----
$V_{Ba}^{//}$	3.45	2.76
$V_O^{\bullet\bullet}$	0.62	0.45 – 0.68

Because interstitial defects are unfavorable, the Schottky disorder is preferred for intrinsic defects [54]:

$$\text{nil} \rightarrow V_{Ba}^{//} + V_{Ti}^{////} + 3V_O^{\bullet\bullet} \qquad (2.1)$$

Depending on the principle mechanism used to compensate these defects, the defect state of $BaTiO_3$ can be broken down into several regimes: reducing, oxidizing and intermediate. These mechanisms are illustrated in Figure 2.4.

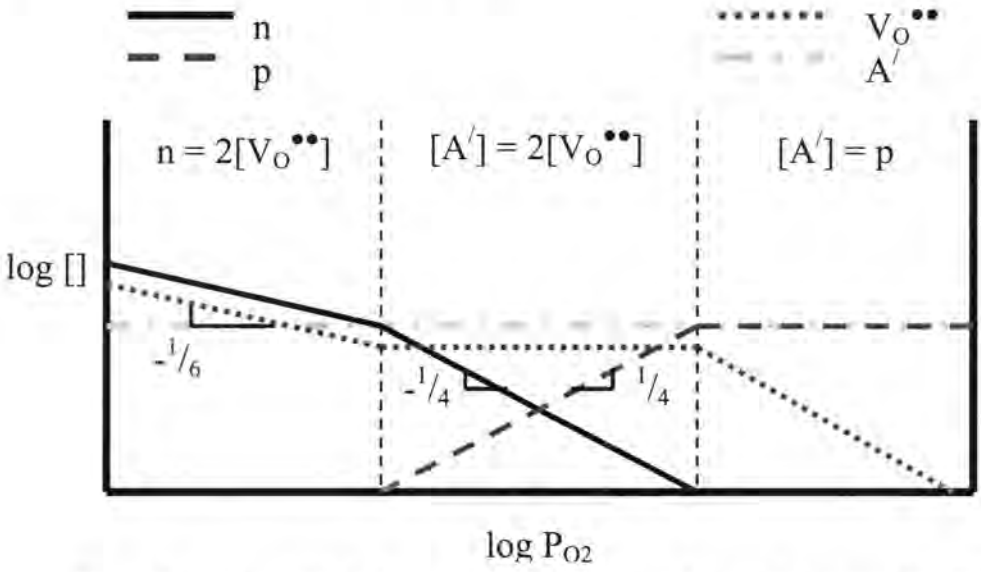

Figure 2.4: Kröger-Vink diagram illustrating the defect mechanisms of $BaTiO_3$

Several models have been proposed to explain the defect behavior of $BaTiO_3$, and a general review can be found in Reference 55. Most models agree on the mechanism for the very low P_{O2} regime in which electrons are generated to compensate for oxygen vacancies giving rise to n-type semiconducting behavior:

$$O_O \rightarrow \tfrac{1}{2}O_2 + V_O^{\bullet\bullet} + 2e^{/} \qquad (2.2)$$

with the electroneutrality expression:

$$2[V_O^{\bullet\bullet}] = n \qquad (2.3)$$

The mechanisms in the oxidizing and intermediate regime are not as easy to isolate. For the high P_{O2} regime, the probable intrinsic reactions possess extremely high enthalpies [54]. This disagrees with the existing data, which shows that conductivity is less dependent on temperature in the high P_{O2} regime then the low P_{O2} regime. In other words, $BaTiO_3$ should be easier to oxidize than to reduce. One explanation is an extrinsic reaction in which defects (oxygen vacancies) are consumed rather than created:

$$\tfrac{1}{2}O_2 + V_O^{\bullet\bullet} \rightarrow O_O + 2h^{\bullet} \qquad (2.4)$$

The extrinsic oxygen vacancies are believed to form in order to compensate for acceptor impurities that occur even in pure $BaTiO_3$. The complete reaction for an acceptor ion (A) substituting for Ba^{2+} under oxidizing conditions would be:

$$A_2O + 2TiO_2 + \tfrac{1}{2}O_2 \rightarrow 2A'_{Ba} + 2Ti_{Ti} + 6O_O + 2h^{\bullet} \qquad (2.5)$$

with electroneutrality expression:

$$\left[A'_{Ba}\right] = p \qquad (2.6)$$

Data for the oxidizing regime is limited due to the instability of $BaTiO_3$ at high P_{O2}.

The intermediate regime is also believed to be due to extrinsic effects in which oxygen vacancies are compensated by acceptor dopants. Again, for an acceptor ion substituting for Ba^{2+}, the reaction would be:

$$A_2O + 2TiO_2 \rightarrow 2A'_{Ba} + 2Ti_{Ti} + 5O_O + V_O^{\bullet\bullet} \qquad (2.7)$$

with electroneutrality expression:

$$2\left[V_O^{\bullet\bullet}\right] = \left[A'_{Ba}\right] \qquad (2.8)$$

Typical conductivity curves for $BaTiO_3$ as a function of P_{O2} are shown in Figure 2.5.

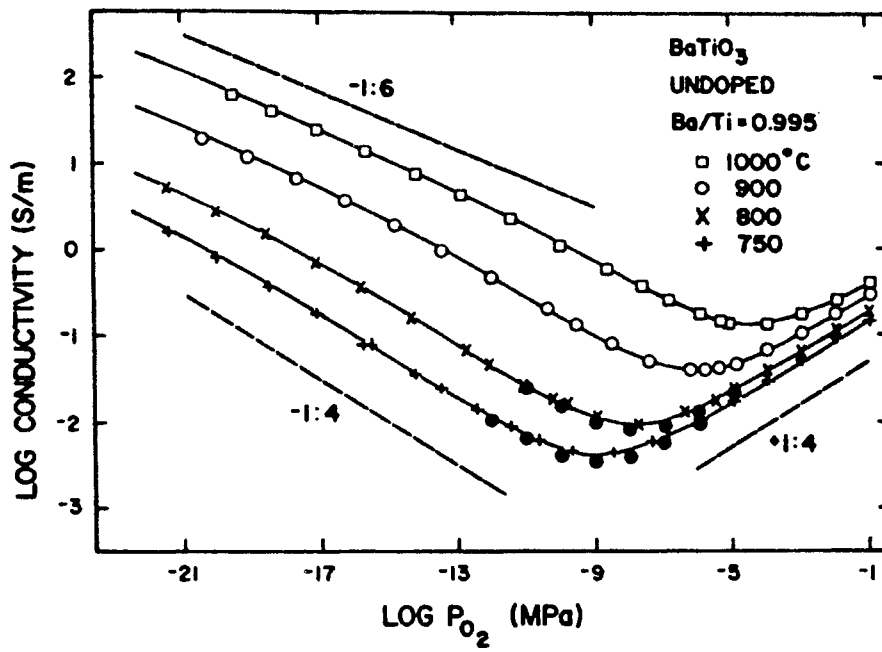

Figure 2.5: The equilibrium electrical conductivity of undoped $BaTiO_3$ as a function of oxygen partial pressure and temperature (taken from Smyth [54])

In order to determine where silver will enter the perovskite structure it is important to examine the ionic radii (Table 2.3). As the radius of Ag^+ is much larger than the radius of Ti^{4+}, it is expected that Ag^+ will substitute for Ba^{2+}. However, studies conducted on the introduction of Ca^{2+} into the $BaTiO_3$ lattice have shown that Ca^{2+} will replace Ti^{4+} when Ba:Ti >1 [15, 21, 64].

Table 2.3: Ionic radii of Ba, Ag, Ti and Ca ions[29]

Ion	Radius (Å)*
Ba^{2+}	1.49 (1.75)
Ag^+	1.29
Ti^{4+}	0.75
Ca^{2+}	1.14 (1.48)

*radii in parentheses are for 12-fold coordination, all others for 6-fold coordination

Assuming Ag^+ substitutes for Ba^{2+}, it would behave as an acceptor dopant and produce oxygen vacancies at intermediate oxygen partial pressures:

$$Ag_2O + 2TiO_2 \rightarrow 2Ag'_{Ba} + 2Ti_{Ti} + 5O_O + V_O^{\bullet\bullet} \qquad (2.9)$$

If Ag^+ were to substitute for Ti^{4+} a similar reaction would occur:

$$Ag_2O + 2BaO \rightarrow 2Ba_{Ba} + 2Ag'''_{Ti} + 3O_O + 3V_O^{\bullet\bullet} \qquad (2.10)$$

CHAPTER 3: EXPERIMENTAL PROCEDURE

3.0 Material Preparation

Powders were made with the compositions shown in Table 3.1. The $BaTiO_3$ source material was donated by Ferro Co. (Lot # 992050) with the chemical composition and properties shown in Table 3.2. The source material for silver was $AgNO_3$ (Fisher Scientific, Lot # 007139) and for BaO was $BaCO_3$ (Fisher Scientific, Lot # 934559A). TiO_2 from Fisher Scientific (Lot #973995) was used for the excess TiO_2.

Table 3.1: Compositional matrix of prepared powders

$BaTiO_3$	$BaTiO_3$ + 0.06 mol% Ag	$BaTiO_3$ + 0.1 mol% Ag	$BaTiO_3$+ 0.3 mol% Ag
$BaTiO_3$ + 0.5 mol% BaO	$BaTiO_3$ + 0.5 mol% BaO + 0.06 mol% Ag	$BaTiO_3$ + 0.5 mol% BaO + 0.1 mol% Ag	$BaTiO_3$ + 0.5 mol% BaO + 0.3 mol% Ag
$BaTiO_3$ + 0.5 mol% TiO_2	$BaTiO_3$ + 0.5 mol% TiO_2 + 0.06 mol% Ag	$BaTiO_3$ + 0.5 mol% TiO_2 + 0.1 mol% Ag	$BaTiO_3$ + 0.5 mol% TiO_2 + 0.3 mol% Ag

The powders were made in 50 g batches to ensure that a manageable amount of silver was present. First, the $BaTiO_3$ was calcined in air at 1100°C for four hours in an ATS box furnace (series 3150). For the excess BaO and TiO_2 compositions, the powders were milled in ethanol for five hours on an ASAP vibratory mill with zirconia media prior to calcination. Upon completion of calcination, the $AgNO_3$ was added, and the powders were again milled for five hours on a vibratory mill.

To make pellets, approximately 8 wt% acetone-based binder was added to the powder. The powder was sieved with a #50 mesh and pressed into pellets in a 0.5 inch stainless steel die with a Carver hydraulic press at 2000 and then 3000 psi. The pellets were placed on an alumina plate covered with zirconia powder and fired in a Carbolite tube

furnace in flowing air. Binder burnout occurred at 500°C for two hours and sintering at 1400°C for two hours with a ramp rate of 3°C per minute. Density of the pellets was determined by Archimedes measurements with water as the immersion medium.

Table 3.2: Chemical composition and properties of $BaTiO_3$ as determined by manufacturer

Impurities	**%**
Al_2O_3	0.009
CaO	0.017
Fe_2O_3	0.003
K_2O	0.017
Na_2O	0.027
Nb_2O_5	<0.01
P_2O_5	0.051
SO_3	0.021
SiO_2	0.017
SrO	0.11
ZrO_2	0.009
Properties	
Horiba Particle Size, D50%	1.25 μm
Tap Density	80 lbs/ft^3
Loss on Ignition at 982°C	0.15%
Surface Area	1.93 M^2/g
Acetic Acid Soluble BaO	1.24%
pH at 10% Solids	10.4
(Ba + Sr)O Assay	65.56%
TiO_2 Assay	34.29%
(Ba + Sr):Ti Mole Ratio	0.9968

3.1 Property Measurements

3.1.0 Capacitance Measurements

To prepare the pellets for capacitance measurements, the surface was given a rough polish with 320 grit sandpaper in order to remove any surface contamination. Gold electrodes were sputtered onto the pellets with an Edwards Scancoat Six sputter coater. A

dab of SPI Supplies flash-dry silver paint was placed on top of the electrodes to ensure a good electrical contact.

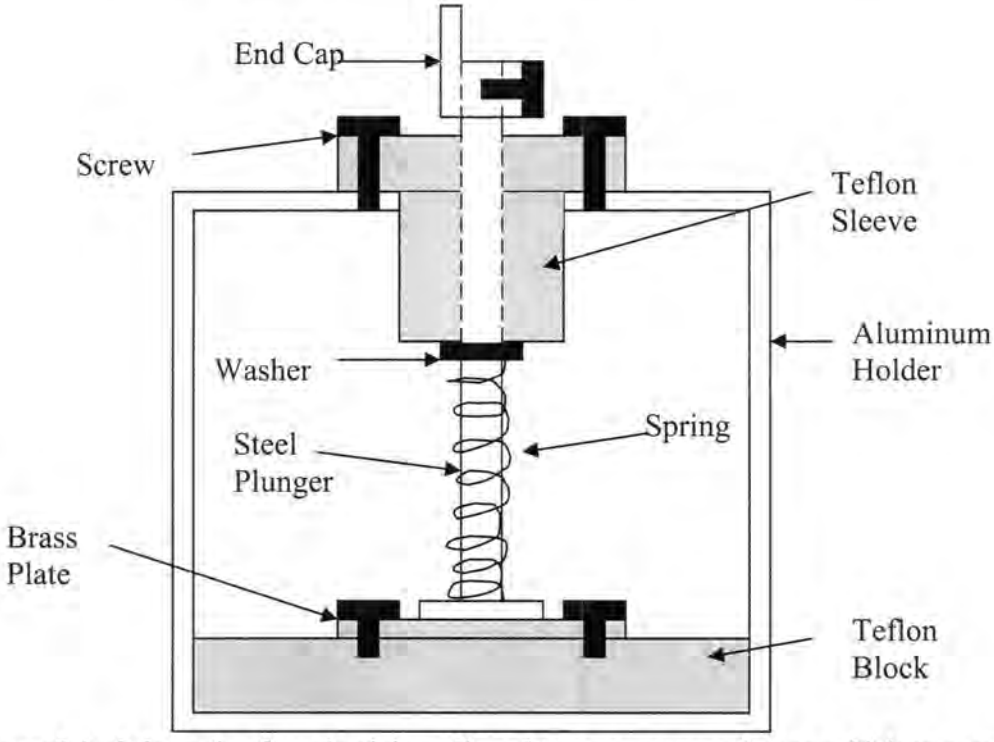

Figure 3.1: Schematic of conductivity cell used to measure capacitance at high temperatures

Capacitance and tan δ measurements were carried out using the conductivity cell shown in Figure 3.1 and a Keithley 3330 LCZ meter. Several pellets of each composition were measured at room temperature at low frequencies (0.12, 1, 10 and 100 kHz) to obtain an average value for each frequency. For the high temperature measurements only the densest pellet of each group was measured. Measurements took place in a Delta Design 9023 temperature chamber starting at 150°C and ending around room temperature. The temperature was measured with an Omega HH12 meter using a type K thermocouple placed near the sample. The capacitance was used to calculate the dielectric constant. The Curie constant (C) and the Curie-Weiss temperature (θ_c) were determined by the Curie-Weiss law

from a graph of K^{-1} vs. temperature. The data obtained at 10 kHz was used for this purpose due to a greater stability in the readings at this frequency.

3.1.1 Lattice Parameter Measurements

Lattice parameter measurements were carried out at room temperature in a Scintag XGEN-4000 x-ray diffractometer (XRD). Sintered pellets were ground to powder and mixed with Strem Chemicals 99.9% pure tungsten powder (Lot # B6808040) at a ratio of 1:5 to act as a standard. Select peaks shown in Figure 3.2 were scanned using CuK_α radiation in the range of 38° - 143° with a step of 0.02° and scan time of 15 seconds per step. Lattice parameters were determined by Cohen's least squares method [65]. The following relationship was used for a tetragonal system:

$$\sin^2\theta = \frac{\lambda^2}{4a^2}\left(h^2 + k^2\right) + \frac{\lambda^2}{4c^2}\left(l^2\right) + \delta\sin\theta\cos^2\theta \qquad (3.1)$$

where δ is the drift constant. Peaks were located using the peak-finder utility in the program WinPLOTR [66].

3.1.2 Grain Size Measurements

Samples were thermally etched at 1300°C for two hours in a Lindberg box furnace in order to delineate the grain structure. Several micrographs were taken of each sample by a Hitachi S-2460N scanning electron microscope (SEM) to provide a good statistical basis. The average intercept length was determined using the circle intercept method outlined by ASTM [67]. From this the average grain size was determined using the equation:

$$G_{av} = kl_{av} \qquad (3.2)$$

where G_{av} is the average grain size, l_{av} is the average intercept length and k is a proportionality constant [68]. For tetrakaidecahedral grains, a model commonly chosen to represent grains in polycrystalline ceramics, k equals 1.558.

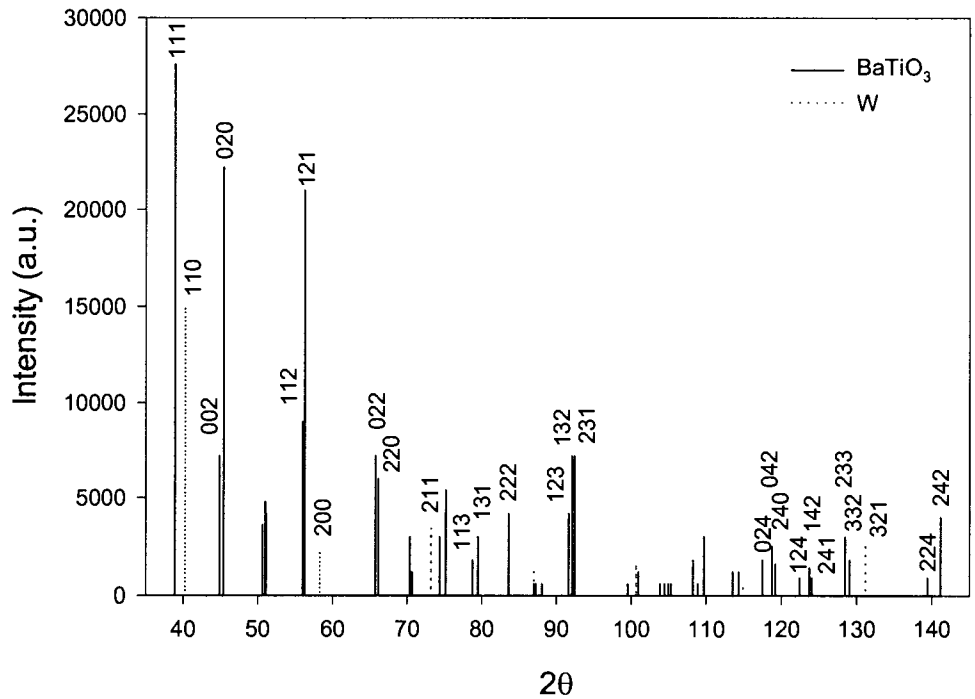

Figure 3.2: Line diffraction pattern of $BaTiO_3$ and W indicating peaks selected for lattice parameter determination

CHAPTER 4: RESULTS

4.0 Electronic Properties

The room temperature dielectric constant (K_{rm}) and dissipation factor (tan δ_{rm}) for stoichiometric $BaTiO_3$ demonstrated little change as silver content increases (Figures 4.1 and 4.2). In addition, there was no noticeable variation in T_c (Table 4.1), which agrees with the results obtained by Chen and Tuan [43]. The Curie-Weiss temperature remained fairly constant as well until 0.3 mol% Ag when it decreased (Figure 4.3). This coincided with a decrease in K_{max} (Table 4.1), which remained relatively stable at lower silver concentrations. Of note is the larger spread of K as a function of frequency above T_c as seen in Figure A.7 in Appendix A (all temperature scans for K and tan δ can be found in Appendix A). This signifies an increase in the space charge effect. Space charge polarization is indicative of mobile charge carriers, in this case induced by high silver concentrations. Its presence is most felt at low frequencies due to the comparatively long diffusion times of the charge carriers. Another sign of the rise in the space charge polarization was observed in the higher tan δ values just above T_c for 0.3 mol% Ag compared to those of lower silver content (Figures A.2, A.4, A.6 and A.8 in Appendix A). This was especially highlighted for the low 0.12 kHz frequency.

In contrast, the dielectric properties of the excess TiO_2 and BaO compositions displayed a greater sensitivity to the presence of silver. The excess BaO compositions demonstrated a minimum in K_{rm} at 0.01 mol% Ag while for excess TiO_2 the minimum occured at 0.06 mol% Ag. An increase in tan δ_{rm} was seen for the excess TiO_2. However, tan δ_{rm} for the excess BaO decreased slightly at 0.06 mol% Ag and then remained constant.

Furthermore, as with the stoichiometric $BaTiO_3$, the spread of K over the different frequencies was larger for the excess TiO_2 composition with the 0.3 mol% Ag addition (Figure A.15 in Appendix A). Again, this was accompanied by a larger tan δ above T_c (Figure A.16 in Appendix A). Conversely, this phenomenon was not present in the excess BaO (Figures A.23 and A.24 in Appendix A). A minor decrease in T_c was observed for excess TiO_2 at 0.06 mol% Ag after which no change was seen. For excess BaO, both T_c and θ_c remained constant.

As seen in Figure 4.4, the Curie constant decreased for all compositions until it reached a minimum at 0.1 mol% Ag. The order of magnitude is in agreement with previously reported results [11, 12, 39, 69].

Table 4.1: Results of capacitance measurements of $BaTiO_3$ as a function of composition*

mol% Ag	T_c† (°C)	θ_c (°C)	C (°C x 10^5)	K_{rm}	K_{max} (x 10^3)	tan δ_{rm}
$BaTiO_3$						
0	125	109	1.53	1400 ± 70	9.56	0.0099 ± 0.0005
0.06	125	110	1.50	1450 ± 70	10.0	0.0114 ± 0.0004
0.1	124	110	1.48	1490 ± 70	10.1	0.013 ± 0.001
0.3	124	104	1.63	1450 ± 60	7.97	0.009 ± 0.002
$BaTiO_3$ + 0.5 mol% TiO_2						
0	125	106	1.55	1540 ± 60	7.98	0.009 ± 0.001
0.06	123	106	1.40	1280 ± 30	8.31	0.0166 ± 0.0007
0.1	123	109	1.37	1380 ± 20	9.13	0.019 ± 0.004
0.3	123	103	1.46	1320 ± 30	7.35	0.0145 ± 0.0005
$BaTiO_3$ + 0.5 mol% BaO						
0	124	110	1.65	1680 ± 10	10.9	0.0136 ± 0.0006
0.06	123	109	1.46	1500 ± 50	9.46	0.0110 ± 0.0003
0.1	124	111	1.41	1400 ± 50	10.4	0.0111 ± 0.0004
0.3	123	109	1.44	1490 ± 20	10.1	0.0080 ± 0.0009

* reported data collected at 10 kHz
† error from instrument ± 1°C

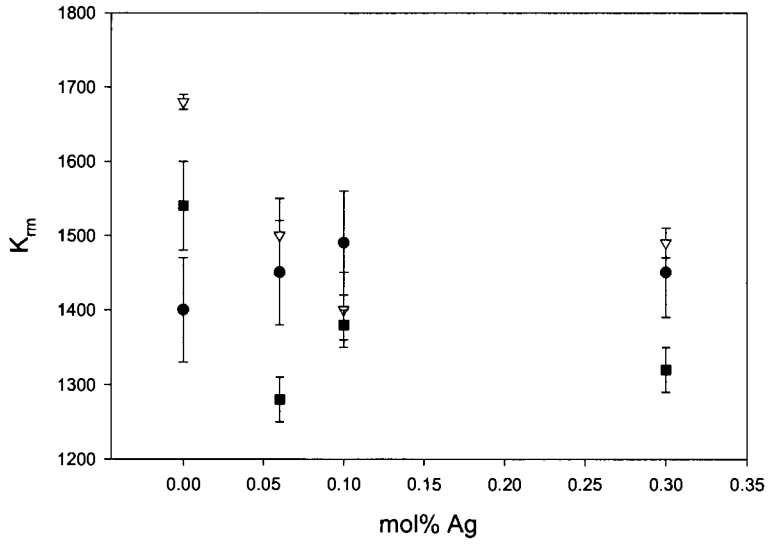

Figure 4.1: K_{rm} as a function of silver concentration for $BaTiO_3$ (●), $BaTiO_3$ + 0.5 mol% BaO (▽) and $BaTiO_3$ + 0.5 mol% TiO_2 (■) at 10 kHz

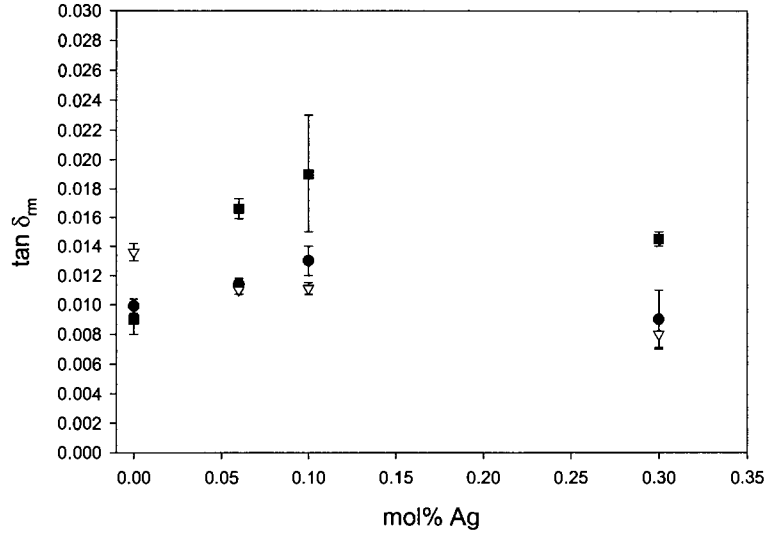

Figure 4.2: tan δ_{rm} as a function of silver concentration for $BaTiO_3$ (●), $BaTiO_3$ + 0.5 mol% BaO (▽) and $BaTiO_3$ + 0.5 mol% TiO_2 (■) at 10 kHz

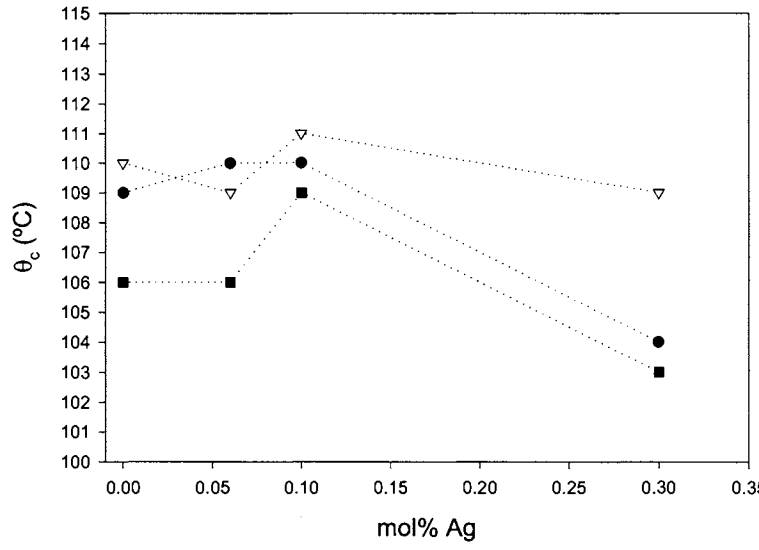

Figure 4.3: θ_c as a function of silver concentration for $BaTiO_3$ (●), $BaTiO_3$ + 0.5 mol% BaO (▽) and $BaTiO_3$ + 0.5 mol% TiO_2 (■) at 10 kHz

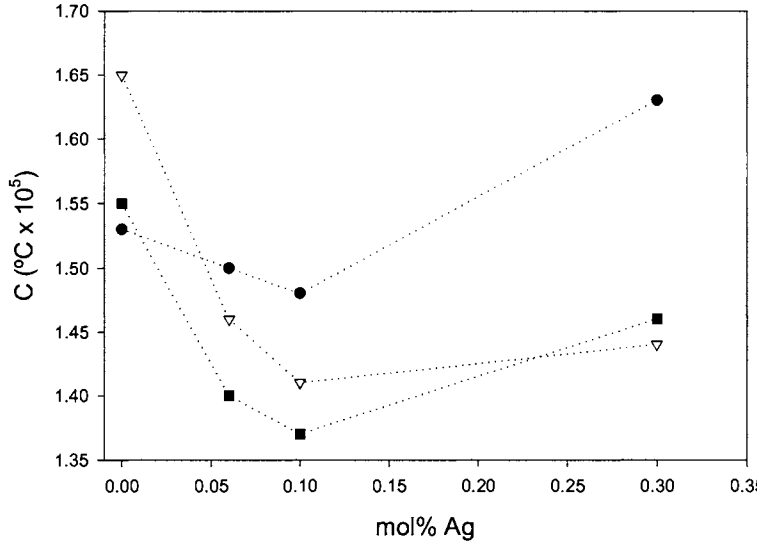

Figure 4.4: C as a function of silver concentration for $BaTiO_3$ (●), $BaTiO_3$ + 0.5 mol% BaO (▽) and $BaTiO_3$ + 0.5 mol% TiO_2 (■) at 10 kHz

4.1 Lattice Parameters

For the stoichiometric composition, no change was observed in the lattice parameters as silver concentration increased (Figures 4.5 and 4.6). This was not found to be true for the excess compositions. For the excess TiO_2 composition, **a** increased and **c** decreased at 0.06 mol% Ag. This lowered the **c/a** ratio, as seen in Figure 4.7, indicating that the material was less tetragonal. The decrease in the **c/a** ratio coincided with an increase in the unit cell volume (V) as seen in Figure 4.8. Above 0.06 mol% Ag, the lattice parameters stabilized.

The opposite behavior was observed for the excess BaO compositions; **a** decreased and **c** increased at 0.06 mol% Ag. This increased the **c/a** ratio indicating the material was more tetragonal. At the same time, there was a decrease in V. Again the lattice parameters stabilized above 0.06 mol% Ag except for **a**, which increased at 0.3 mol% Ag.

The standard deviation obtained from the tungsten standard was 0.0002 Å. All drift constants (δ) were on the order of 10^{-5}. XRD scans are compiled in Appendix B.

Table 4.2: Results of lattice parameter measurements of $BaTiO_3$ as a function of composition

$BaTiO_3$					
mol% Ag	**a (Å)**	**c (Å)**	**δ ($x10^{-5}$)**	**c/a**	**V ($Å^3$)**
0	3.9938	4.0354	-5.79	1.0104	64.365
0.06	3.9937	4.0352	-7.36	1.0104	64.362
0.1	3.9939	4.0354	-7.08	1.0104	64.371
0.3	3.9941	4.0351	-4.28	1.0103	64.372
$BaTiO_3$ + 0.5 mol% TiO_2					
0	3.9942	4.0359	-6.55	1.0104	64.386
0.06	3.9949	4.0350	-5.65	1.0100	64.396
0.1	3.9949	4.0351	-5.89	1.0101	64.397
0.3	3.9949	4.0349	-7.54	1.0100	64.395
$BaTiO_3$ + 0.5 mol% BaO					
0	3.9960	4.0345	-4.15	1.0096	64.421
0.06	3.9944	4.0352	-4.95	1.0102	64.382
0.1	3.9944	4.0351	-2.55	1.0102	64.380
0.3	3.9949	4.0349	-7.57	1.0100	64.395

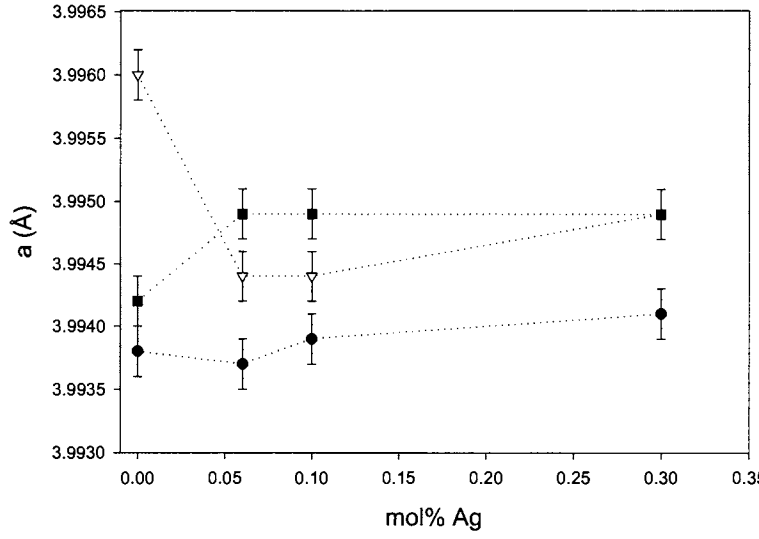

Figure 4.5: Lattice parameter, **a**, as a function of silver concentration for $BaTiO_3$ (●), $BaTiO_3$ + 0.5 mol% BaO (▽) and $BaTiO_3$ + 0.5 mol% TiO_2 (■)

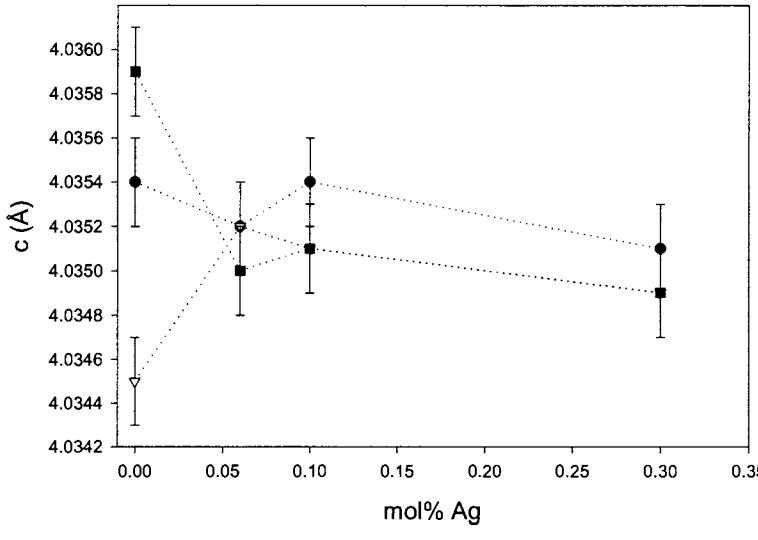

Figure 4.6: Lattice parameter, **c**, as a function of silver concentration for $BaTiO_3$ (●), $BaTiO_3$ + 0.5 mol% BaO (▽) and $BaTiO_3$ + 0.5 mol% TiO_2 (■)

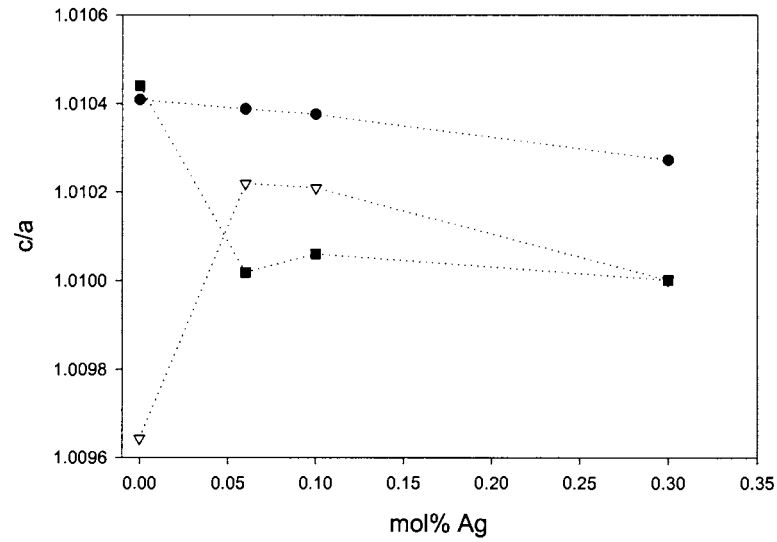

Figure 4.7: **c/a** as a function of silver concentration for $BaTiO_3$ (●), $BaTiO_3$ + 0.5 mol% BaO (▽) and $BaTiO_3$ + 0.5 mol% TiO_2 (■)

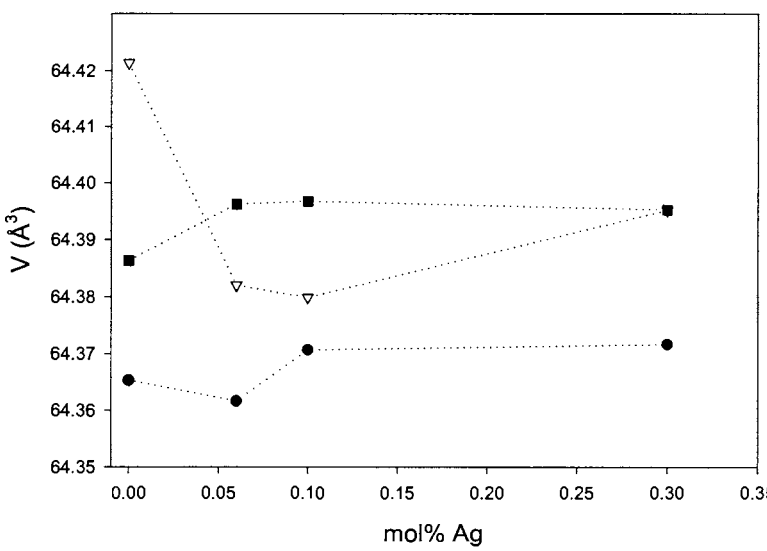

Figure 4.8: V as a function of silver concentration for $BaTiO_3$ (●), $BaTiO_3$ + 0.5 mol% BaO (▽) and $BaTiO_3$ + 0.5 mol% TiO_2 (■)

4.2 Microstructure

All samples were tan in color. Large grains could be seen on the surface of the $BaTiO_3$ + 0.5 mol% TiO_2 sample. Fracturing the pellets revealed a discoloration in the center of the pellets for the 0.3 mol% Ag samples (Figure 4.9). The discoloration was surrounded by the lighter tan color and gave the appearance of a depletion zone yet electron dispersive spectrometry (EDS) detected no significant change in composition between the dark center and lighter outer layer. Due to the small amount of silver used, this is not surprising. The discoloration was more diffuse in the excess TiO_2 sample compared to the other compositions.

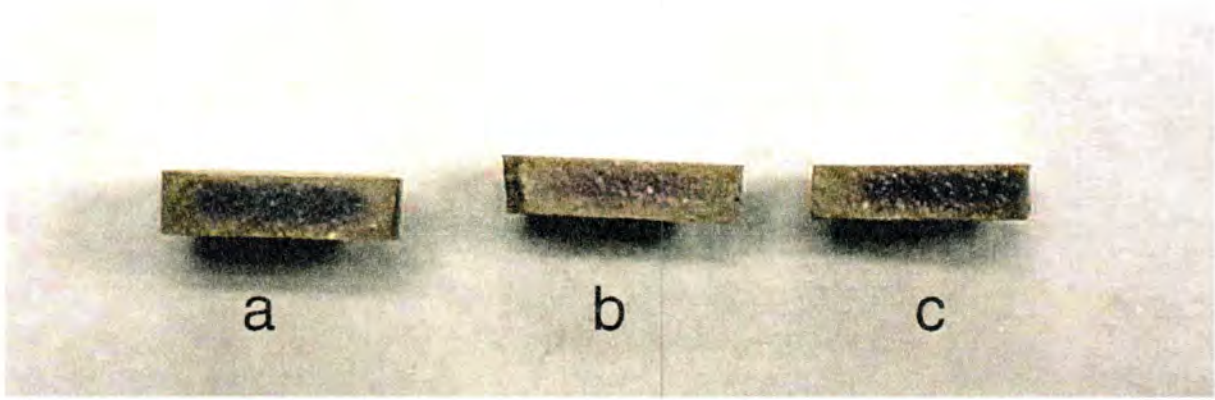

Figure 4.9: Fracture surface of pellets containing 0.3 mol% Ag for (a) $BaTiO_3$, (b) $BaTiO_3$ + 0.5 mol% TiO_2 (c) and $BaTiO_3$ + 0.5 mol% BaO

Chemical analysis of the pellets was conducted to determine the silver content using inductively coupled plasma (ICP) methods. It was largely unsuccessful due to an inability to completely dissolve the samples. However, no silver was detected in the material that did go into solution. X-ray fluorescence (XRF) was also used to determine the silver content of the pellets. Again, no trace of silver was detected with the detector limit being 30 ppm. This presents two possibilities. The first is that the silver completely volatized during firing. A

not unreasonable supposition considering the high firing temperature (1400°C) compared to the inherent volatility and low melting temperature of silver (960°C). The second possibility is that the silver is present in concentrations below 30 ppm. The space charge effect apparent in the 0.3 mol% Ag samples would indicate that some silver is present in these samples at least and could be the source of the observed discoloration.

From Figure 4.10 it can be seen that the presence of silver played a significant role on the grain size of $BaTiO_3$. Stoichiometric $BaTiO_3$ showed little variation in grain size except for a sudden drop at 0.06 mol% Ag after which it returned to its former size (Figures 4.11-15). Occasional clusters of small grains were observed for the 0.06 mol% Ag sample (Figure 4.14). Also of note was that the grain boundaries were more disticint in the samples that contained silver indicating the presence of a secondary phase, probably silver, along the grain boundaries during sintering. $BaTiO_3$ with excess TiO_2 experienced a dramatic decrease in grain size at 0.06 mol% Ag and then stabilized (Figures 4.16-19). The opposite behavior was observed for excess BaO with grain size increasing at 0.06 mol% Ag after which it remained constant (Figures 4.20-4.23).

As seen in Figure 4.16 the excess TiO_2 sample with no silver additions displayed the formation of extremely large abnormal grains. Such large grains have been previously reported [70, 71] and are partially attributed to the presence of a liquid phase. The excess TiO_2 forms a secondary phase ($Ba_6Ti_{17}O_{40}$) that develops a eutectic liquid with $BaTiO_3$ at 1332°C, well below the sintering temperature of 1400°C [72, 73]. The promotion of sintering also accounts for the higher density of the sample compared to the other compositions (Figure 4.11). Upon the addition of silver these large grains completely disappeared (Figure 4.17). This was accompanied by a reduction in the density.

Very small grains, on the order of a few microns, were dispersed throughout the $BaTiO_3$ + 0.5 mol% BaO sample (Figure 4.21). Former studies have noted that BaO acts as a grain size refiner [70, 74]. Large porous cavities were also apparent and explain the lower density of the sample. At higher silver concentrations the small grains are no longer evident (Figures 4.22-24). The porous cavities disappeared with the addition of silver as well. This was attended by an increase in density.

Table 4.3: Results of grain size and density measurements of $BaTiO_3$ as a function of composition

mol% Ag	G_{av} (μm)	95% CI (μm)	% RA	ρ (g/cm^3)	% dense
$BaTiO_3$					
0	54 ± 4	3.58	6.7	5.73 ± 0.04	95.3
0.06	33 ± 4	2.92	8.8	5.77 ± 0.04	96.0
0.1	53 ± 3	2.40	4.5	5.75 ± 0.03	95.6
0.3	52 ± 2	1.42	2.7	5.71 ± 0.04	95.0
$BaTiO_3$ + 0.5 mol% TiO_2					
0*	65 ± 2	1.49	2.3	5.80 ± 0.02	96.5
0.06	28.2 ± 0.7	0.55	2.0	5.72 ± 0.08	95.1
0.1	27.2 ± 0.8	0.63	2.3	5.74 ± 0.04	95.5
0.3	25 ± 1	1.08	4.3	5.70 ± 0.05	94.8
$BaTiO_3$ + 0.5 mol% BaO					
0*	28 ± 3	3.29	11.6	5.63 ± 0.03	93.6
0.06	60 ± 4	3.98	5.3	5.70 ± 0.05	94.8
0.1	56 ± 2	1.81	3.2	5.68 ± 0.03	94.5
0.3	58 ± 2	1.29	2.2	5.68 ± 0.03	94.5

CI: confidence interval, RA: relative accuracy

* grain size measurements for matrix grains and do not account for the abnormally large or small grains

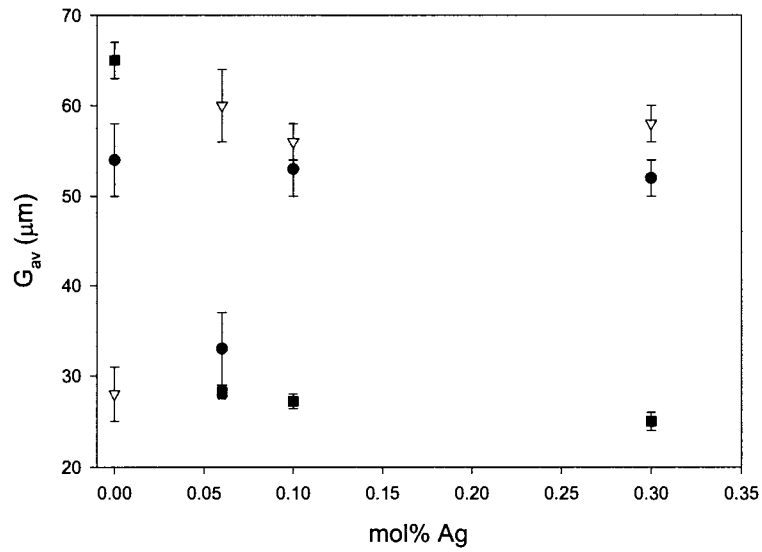

Figure 4.10: Average grain size as a function of silver concentration

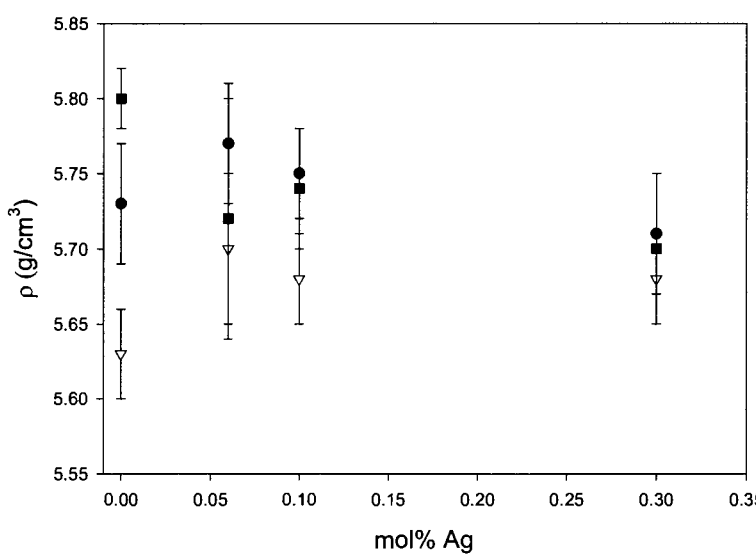

Figure 4.11: ρ as a function of silver concentration for $BaTiO_3$ (●), $BaTiO_3$ + 0.5 mol% BaO (▽) and $BaTiO_3$ + 0.5 mol% TiO_2 (■)

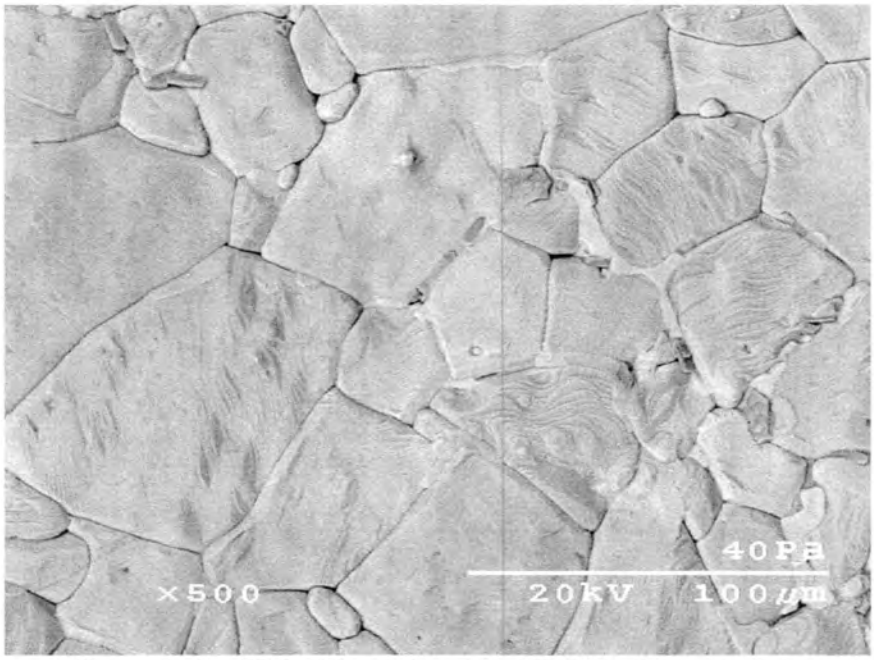

Figure 4.12: SEM of thermally etched $BaTiO_3$ microstructure

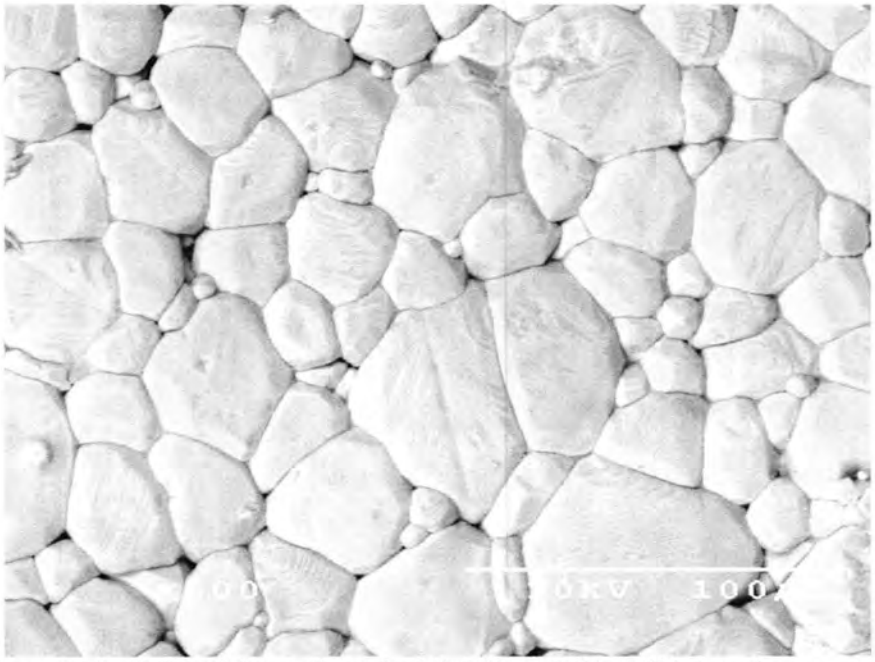

Figure 4.13: SEM of thermally etched $BaTiO_3$ + 0.06 mol% Ag microstructure

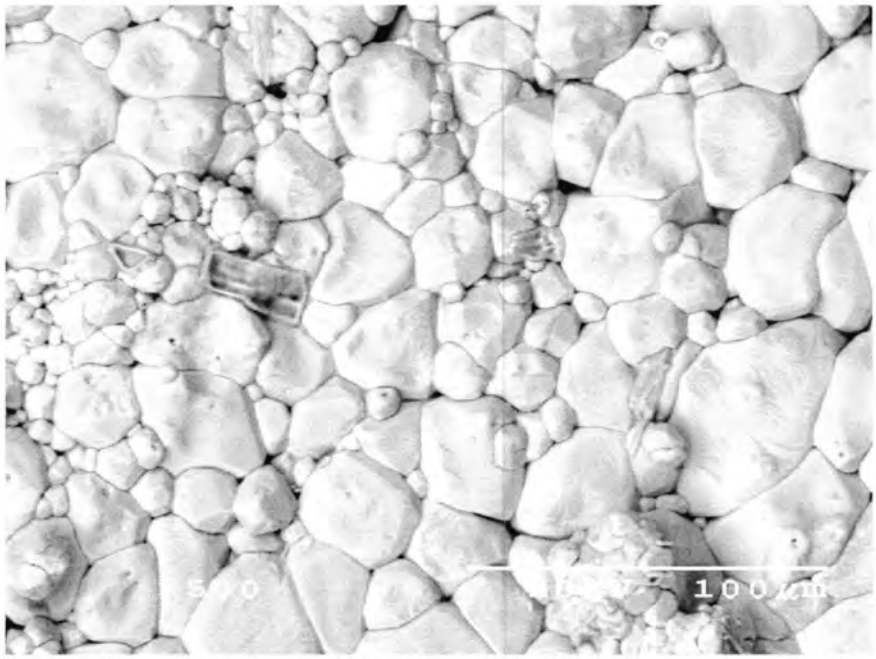

Figure 4.14: SEM of thermally etched $BaTiO_3$ + 0.06 mol% Ag microstructure showing local cluster of small grains

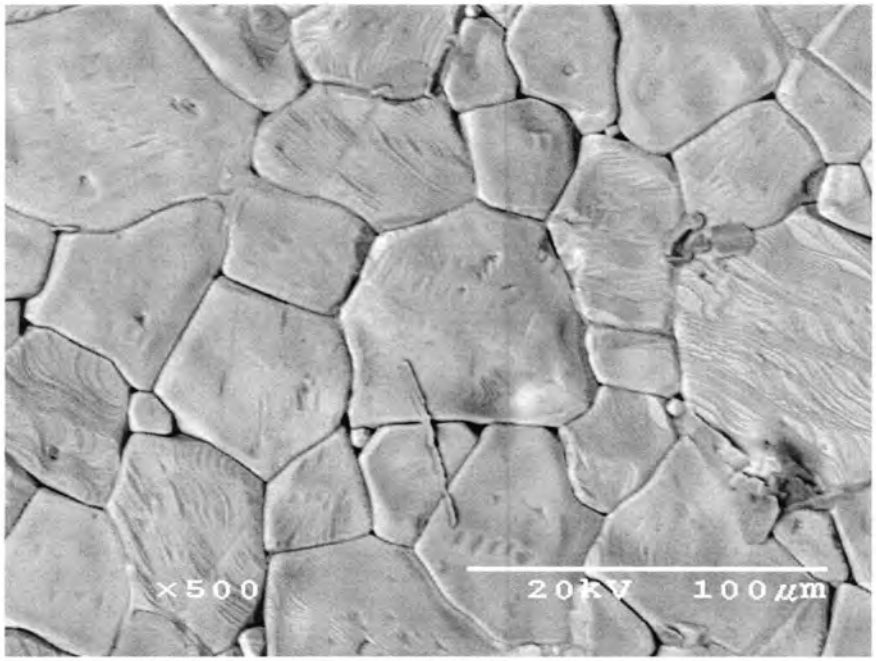

Figure 4.15: SEM of thermally etched $BaTiO_3$ + 0.1 mol% Ag microstructure

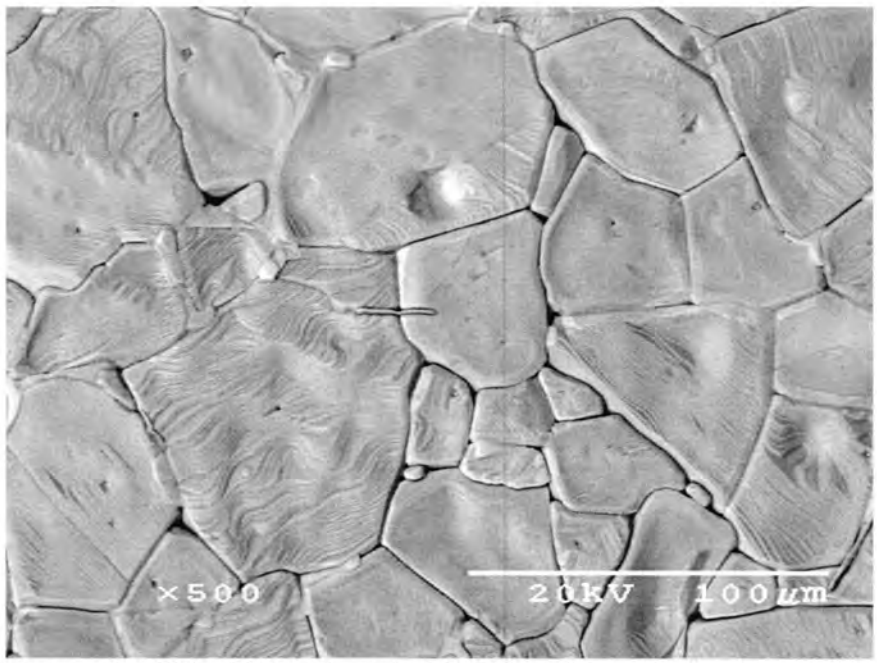

Figure 4.16: SEM of thermally etched $BaTiO_3$ + 0.3 mol% Ag microstructure

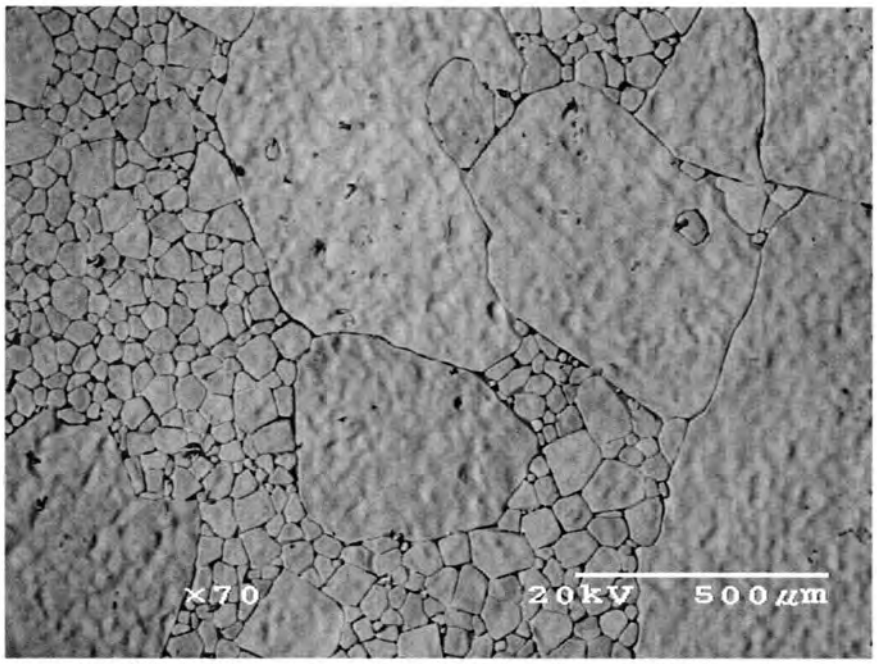

Figure 4.17: SEM of thermally etched $BaTiO_3$ + 0.5 mol% TiO_2 microstructure

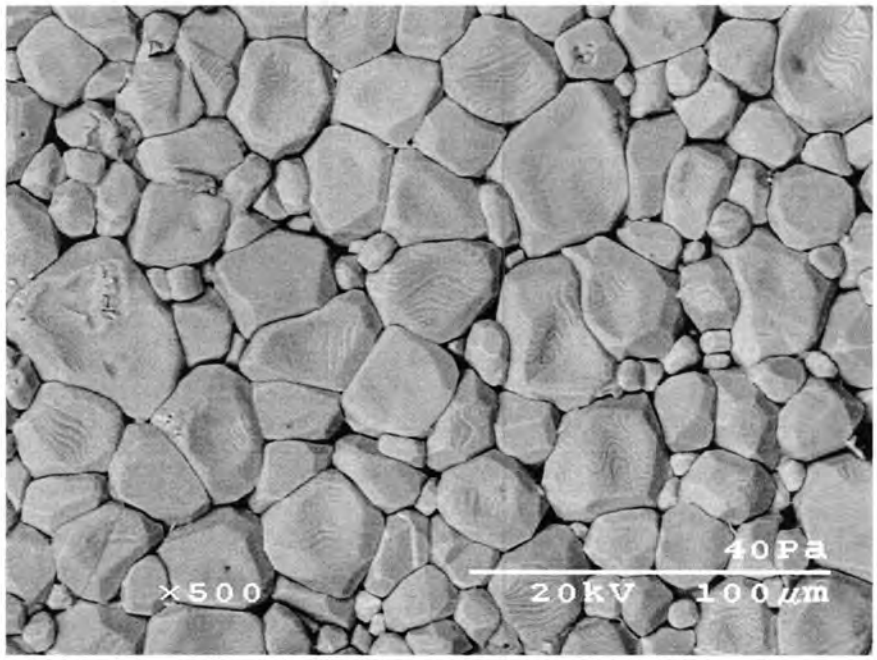

Figure 4.18: SEM of thermally etched $BaTiO_3$ + 0.5 mol% TiO_2 + 0.06 mol% Ag microstructure

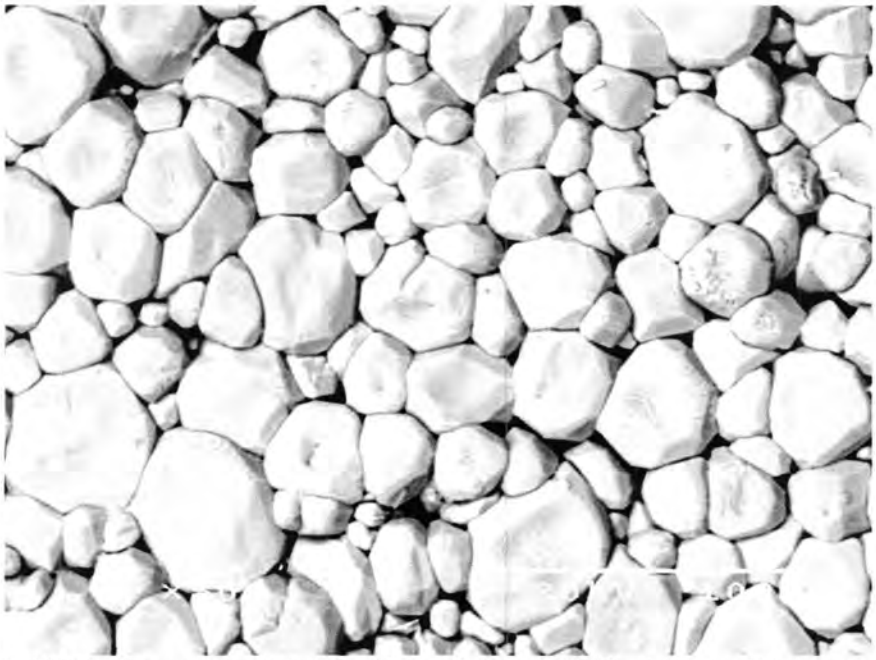

Figure 4.19: SEM of thermally etched $BaTiO_3$ + 0.5 mol% TiO_2 + 0.1 mol% Ag microstructure

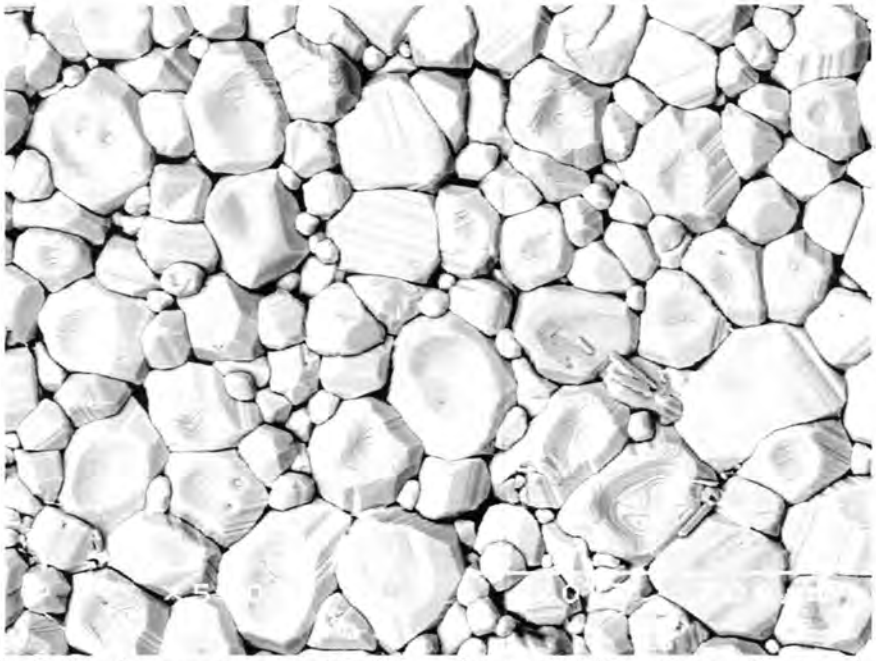

Figure 4.20: SEM of thermally etched $BaTiO_3$ + 0.5 mol% TiO_2 + 0.3 mol% Ag microstructure

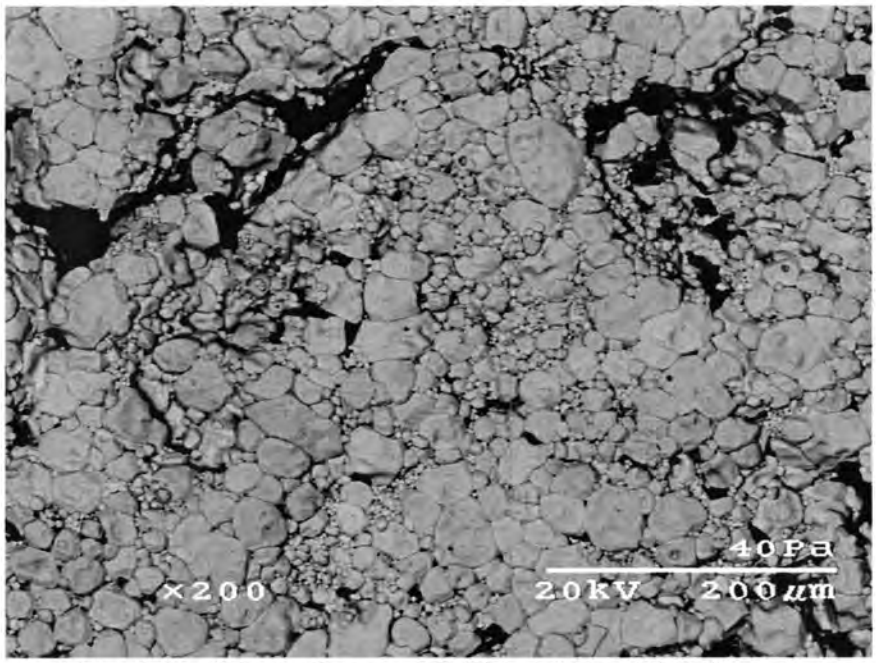

Figure 4.21: SEM of thermally etched $BaTiO_3$ + 0.5 mol% BaO microstructure

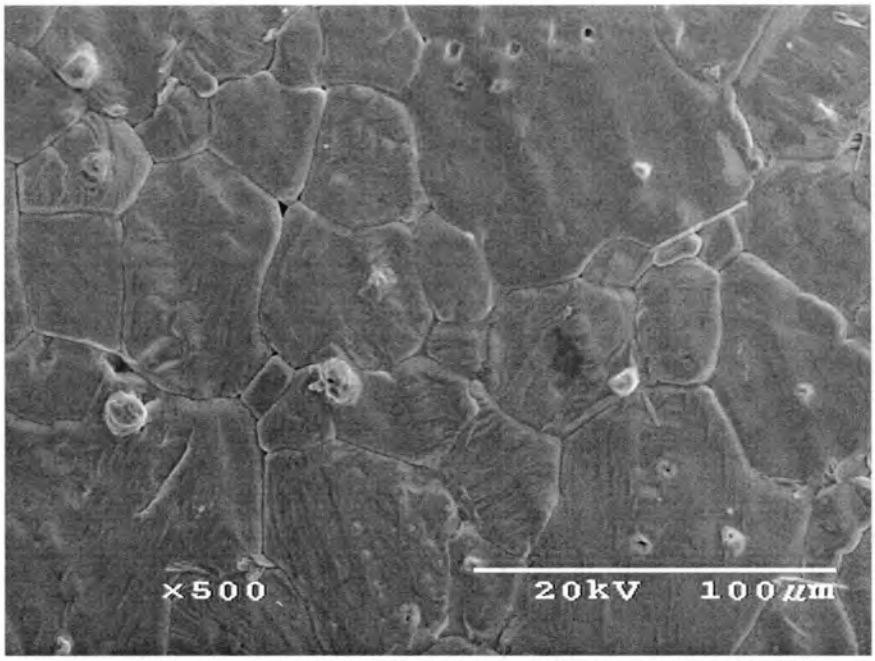

Figure 4.22: SEM of thermally etched $BaTiO_3$ + 0.5 mol% BaO + 0.06 mol% Ag microstructure

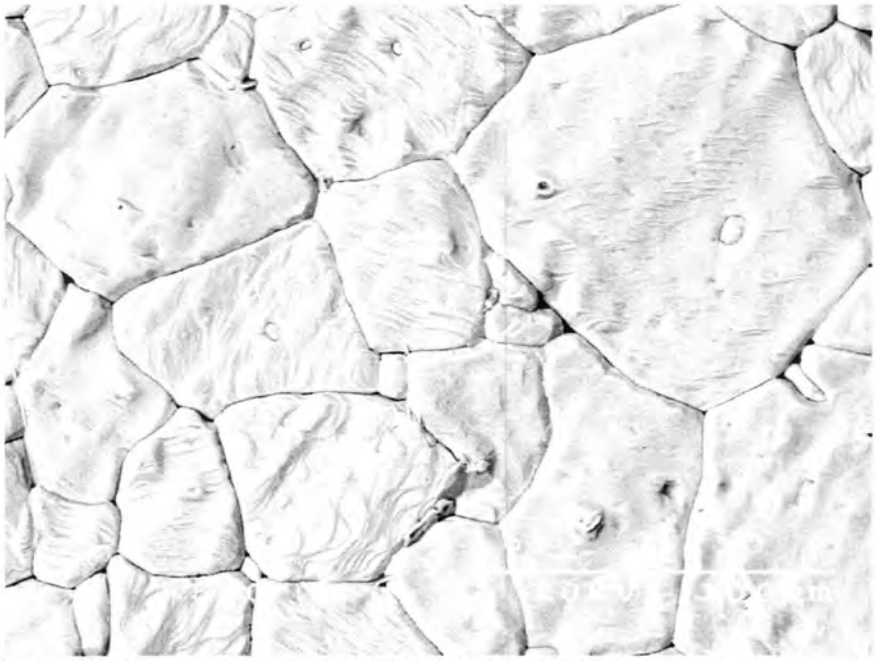

Figure 4.23: SEM of thermally etched $BaTiO_3$ + 0.5 mol% BaO + 0.1 mol% Ag microstructure

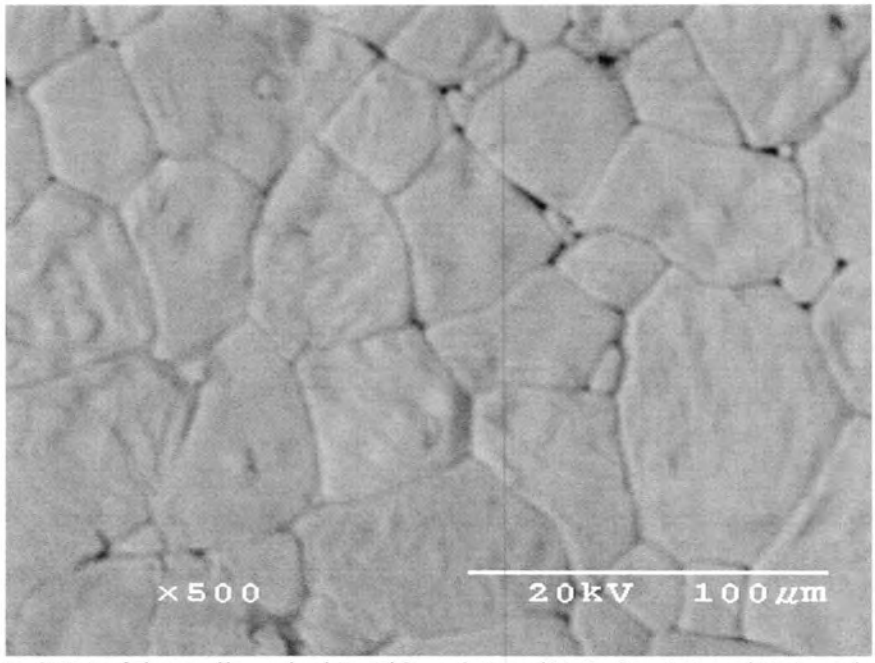

Figure 4.24: SEM of thermally etched $BaTiO_3$ + 0.5 mol% BaO + 0.3 mol% Ag microstructure

CHAPTER 5: DISCUSSION

5.0 Trend Overview

From the data presented in Chapter 4, a number of trends can be identified as summarized in Table 5.1. Silver additions had little effect on the physical properties of stoichiometric $BaTiO_3$. For $BaTiO_3$ compositions with a 0.5 mol% TiO_2 excess, there was a significant decrease in grain size, the dielectric constant, and density and a minor decrease in the Curie temperature and unit cell volume. For $BaTiO_3$ compositions with a 0.5 mol% BaO excess, there was a significant increase in grain size and density but a considerable decrease in the dielectric constant. There was a minor decrease in the unit cell volume as well.

Table 5.1: Summary of silver effects on $BaTiO_3$ based on composition

Property	Stoichiometric	Excess TiO_2	Excess BaO
Grain Size	no effect	decrease	increase
Dissipation Factor	no effect	increase	no effect
Dielectric Constant	no effect	decrease	decrease
Curie Temperature	no effect	minor decrease	no effect
Density	no effect	decrease	increase
Unit Cell Volume	no effect	minor increase	minor decrease

In the sections below, these effects will be rationalized in terms of the relevant atomistic and microstructural mechanisms that influence these physical properties. Of particular importance is the fact that the lattice parameters showed only minor changes with the addition of silver. In addition, the chemical analysis and XRF results on the sintered sample suggest that the overall silver concentration in the samples is extremely small (less than 30 ppm). Therefore, the physical properties must be either: (i) highly sensitive to small concentrations of silver, or (ii) strongly influenced by the transitory presence of Ag during the sintering process. Even though the concentration of other impurities present in the raw

materials are comparable to the upper limit of the silver concentration (see Table 3.2), $BaTiO_3$ has proven to be highly sensitive to the presence of dopants. Just 0.8 mol% of dysprosium is enough to reduce T_c to room temperature and to raise the dielectric constant [2].

5.1 Silver Solubility

In many oxide systems the solubility can be strongly influenced by non-stoichiometry. From the dielectric, microstructural, and XRD data there is evidence that the solubility of silver in $BaTiO_3$ is also dependent on the stoichiometry. For the stoichiometric compositions silver solubility appears to be negligible, yet both excess TiO_2 and BaO compositions appear to promote the incorporation of minute amounts of silver into the $BaTiO_3$ lattice. To discover the mechanism behind this an examination of the defect chemistry for the excess compositions is required.

For excess TiO_2, Hwang and Han [8] determined that the dominant defect reaction is:

$$TiO_2 \rightarrow V''_{Ba} + Ti_{Ti} + V_O^{\bullet\bullet} + 2O_O \qquad (5.1)$$

Of primary interest is the formation of barium vacancies. On the assumption that silver will preferentially substitute for barium, the increase in concentration of barium vacancies would greatly enhance the number of available substitution sites. The small increase in cell volume might be an indication of the incorporation of silver.

The dependence of silver solubility on the presence of barium vacancies would also account for the lack of silver incorporation in stoichiometric $BaTiO_3$. The formation of barium vacancies has been reported to be the least energetically favorable [62]. Therefore

their intrinsic concentration would be low and would not substantially contribute to silver incorporation. The presence of barium vacancies would be further reduced by the background impurity concentration, which is mainly composed of acceptors. Both previous studies conducted by Chen and Tuan [43] and Ikushima and Hayakawa [52] were made using stoichiometric $BaTiO_3$, and they also detected no change in the lattice parameters. In addition, Ikushima and Hayakawa noted that the resistivity of samples fired in nitrogen experienced a minimum resistivity at Ba:Ti = 0.998 (Figure 5.1) [52].

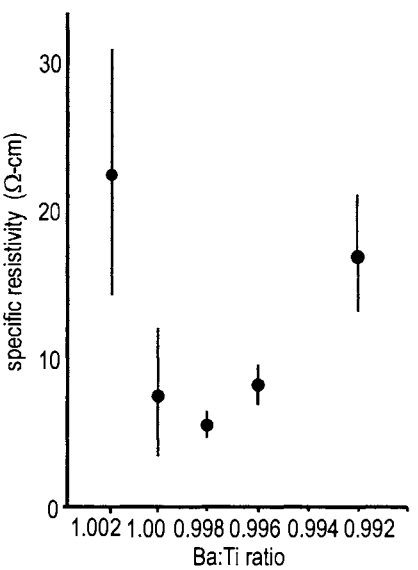

Figure 5.1: Resistivity as a function of nonstoichiometry for $BaTiO_3 + 0.001x\ Ag_2O \pm x\ TiO_2$ (taken from Ikushima and Hayakawa [52])

Consequently, the incorporation of silver would then be limited by the solubility of TiO_2 in $BaTiO_3$, which is not appreciative (~300 ppm) [8]. This explains the limited silver substitution (< 0.06 mol% Ag) for once the solubility limit of TiO_2 is reached very few barium vacancies will be formed for silver occupation. As a result higher concentrations of silver would have no effect on the $BaTiO_3$ crystal structure and, indeed, the lattice parameters for excess TiO_2 remain constant for increased silver content.

A similar mechanism is possible for excess BaO for which the most probable defect reaction is:

$$BaO \rightarrow Ba_{Ba} + V_{Ti}^{////} + O_O + 2V_O^{\bullet\bullet} \qquad (5.2)$$

From Equation 5.2 it can be seen that titanium vacancies are formed. While it is known that Ca^{2+} (1.14 Å) can occupy the B-site when Ba:Ti ratio is greater than unity, the ionic radius of Ag^{+} (1.29 Å) is much greater then for Ti^{4+} (0.75 Å). Therefore it seems unlikely that silver can substitute for titanium. Also, it is unclear whether the decrease in cell volume noted for these compositions has any relationship to silver incorporation. However, from the defect reaction given in Equation 2.10, for every silver ion substituted on a titanium site three oxygen vacancies must be formed to maintain charge neutrality. The loss of the large oxygen ions (1.26 Å) would have a great impact on the lattice and could be the source of the observed shrinkage. Again, if silver were to substitute for titanium the solubility of silver would be limited by that of BaO, which has a lower solubility limit (< 100 ppm) then TiO_2 [8, 74].

5.2 Grain Growth

Silver was found to have a substantial effect on the grain growth behavior of $BaTiO_3$ especially for the nonstoichiometric compositions. First, excess TiO_2 compositions experienced a dramatic decrease in grain size with the addition of silver along with the complete disappearance of abnormal grain growth. It can be concluded that silver is reducing the grain boundary mobility (M_b) and acting as a grain growth inhibitor. In the past, grain growth inhibition has been attributed to a number of causes for acceptor dopants. For

example, research conducted by Čeh and Kolar [75] on the doping of Ca^{2+} into $BaTiO_3$ determined that the formation of a second phase ($Ba_3Ca_2Ti_2O_9$) along the grain boundaries was responsible for grain boundary pinning. Another study by Rahaman [76] postulated that the solute drag effect was the cause of grain growth inhibition for Co^{2+} dopants.

It is unlikely that the mechanism observed by Čeh and Kolar is occurring in this case. First, no secondary phases were detected along the grain boundaries by SEM in any of the sintered samples. Still, this is not conclusive as they may have been present during microstructural evolution. Also the original concentration of silver used was extremely small and the firing temperature very high. Nonetheless, if M_b was reduced by insoluble silver in the grain boundaries one would expect to see a reduction in grain size for all compositions with grain size decreasing with increasing silver content. This does not occur until a much higher silver concentration (> 0.3 wt% Ag) as noted by Chen and Tuan in Figure 2.1 [43].

Examination of the solute drag effect gives a more likely explanation. In this phenomenon dopant ions segregate to the grain boundaries typically in a nonuniform distribution. As the grain boundary moves, the dopant concentration around the grain boundary becomes asymmetrical and exerts a drag force on the grain boundary thus impeding grain growth [38]. According to the Cahn model [77], M_b is dependent on the diffusivity of the dopant ion (D), the concentration of the dopant ion in the grain boundary (C) and the temperature (T):

$$M_b \approx \frac{D}{kTC} \qquad (5.3)$$

where k is the Boltzman constant. Because of the low solubility, no diffusion studies of silver into $BaTiO_3$ have been performed. However, barium is reported to have the slowest

self-diffusion rate due to its large ionic radius and the tight packing of the perovskite structure [16]. Therefore it could be expected that D_{Ag} would be also be small and would account for the reduction of M_b even though the concentration of soluble silver is very low. This hypothesis is further strengthened by a study conducted by Chiang and Takagi [78] who noted that, for $BaTiO_3$, acceptor ions have a strong tendency to segregate to the grain boundaries (Figure 5.2). Thus it would be expected that Ag'_{Ba} would concentrate at the grain boundaries and contribute to the solute drag effect. Furthermore, the reduction of M_b would explain the decrease in density observed for $BaTiO_3$ with excess TiO_2 above 0.06 mol% Ag as the solute drag effect would diminish the effectiveness of the liquid phase sintering.

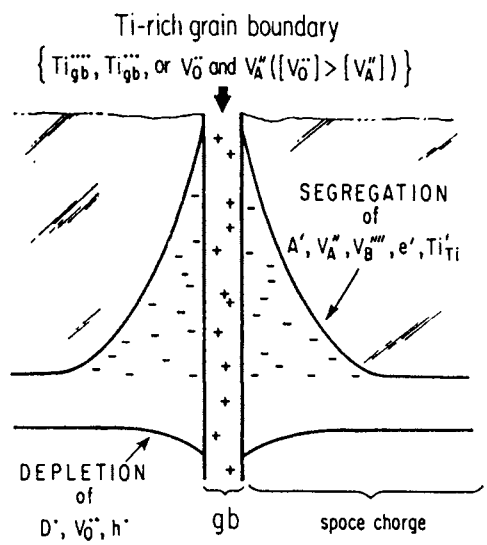

Figure 5.2: Proposed model for grain boundary segregation of charge carries for $BaTiO_3$ (taken from Chiang and Takagi [78])

Unlike excess TiO_2, excess BaO compositions show an increase in grain size and complete suppression of the small abnormal grains and large porous cavities with the addition of silver. Tradition states that a dopant that increases the concentration of the rate-controlling species should enhance grain growth [38]. As self-diffusion is closely linked to vacancy diffusion, examination of the diffusion activation energies listed in Table 2.1

indicates that the rate-controlling species are the cations, especially titanium. Thus a rise in the cation vacancy population should result in larger grains. However, silver incorporation does not add to the cation vacancy population. In fact it does the complete opposite and increases the amount of oxygen vacancies. Then again, anomalous grain growth behavior has been repeatedly reported for donor dopants [2, 9, 19, 76, 71].

Below a critical dopant threshold, usually around 0.5 at%, donor doped $BaTiO_3$ exhibits semiconducting behavior and normal grain growth. Once the dopant threshold is exceeded, the material becomes insulating and a drastic decrease in grain size (~1 μm) is observed. The semiconductor-insulator transition has been attributed to a shift in the defect compensation mechanism from electronic to ionic [9, 79]. For example, $BaTiO_3$ doped with Nb^{5+} below the doping threshold would be compensated by electrons:

$$Nb_2O_5 + 2BaO \rightarrow 2Ba_{Ba} + 2Nb_{Ti}^{\bullet} + 6O_O + \tfrac{1}{2}O_2 + 2e' \qquad (5.4)$$

while above the doping threshold the mechanism is titanium vacancies:

$$BaTiO_3 + 2Nb_2O_5 + 4BaO \rightarrow 5Ba_{Ba} + 4Nb_{Ti}^{\bullet} + V_{Ti}^{////} + 15O_O + TiO_2 \qquad (5.5)$$

From the customary viewpoint, the rise in titanium vacancies above the doping threshold should result in enhanced grain growth, but as already mentioned, the reverse occurs. Because of this it has been proposed that the production of cation vacancies or consumption of oxygen vacancies is responsible for the inhibition in grain growth [76, 9]. Although no mechanism for this has been submitted, support for this theory has been based on the fact that when acceptors are added for donor compensation normal grain growth occurs.

If this theory were correct, it could explain the larger grain size seen in the excess BaO compositions. Assuming silver substitutes on the titanium site, for every incorporated silver ion the result would be the introduction of a large number of oxygen vacancies and the simultaneous elimination of a titanium vacancy. However, no direct evidence for this hypothesis is available at this time.

Another possibility is the development of a sliver flux with the excess BaO although such a compound is unknown. Like the liquid phase sintering that occurs when excess TiO_2 is added to $BaTiO_3$, the flux would aid in the densification process and promote grain growth. As the pellets do become denser when silver is added this possibility must be considered. Silver fluxing alone does not provide enough of an explanation, as its effects should also appear in the other compositions. However, it could be a contributing factor. An alternative option could be that silver influences the surface diffusion. A decrease in the surface diffusion would reduce the pore size, which would increase pore mobility [38]. This encourages densification and grain growth by lowering the amount of pore drag exerted on the grain boundaries. This supposition is supported by the disappearance of the large porous cavities with the addition of silver. Finally, silver could alter the grain boundary energy, or it could be manipulating several of these factors at once. Further study is required to isolate the mechanism behind the enhanced grain growth in excess BaO.

In comparison to the excess compositions, the grain size of stoichiometric $BaTiO_3$ remains constant except for the anomalous decrease observed at 0.06 mol% Ag. As the solubility of silver is insignificant for stoichiometric $BaTiO_3$, solute drag cannot be an issue. The clusters of small grains seen at this silver level indicate the presence of local nonstoichiometry perhaps due to an error in processing. At this time the cause of this

anomalous behavior is unknown but is believed to be due to experimental error. The stable grain size for the other silver concentrations is in accordance with silver's lack of interaction with stoichiometric $BaTiO_3$.

5.3 Dielectric Response

Examination of the dielectric measurements reveals that silver has little effect on the electronic properties of stoichiometric $BaTiO_3$ except for an increase in the space charge effect at 0.3 mol% Ag. This lack of impact can be linked to silver's insolubility, which would result in the concentration of silver along the grain boundaries where much of it would be lost upon sintering due to silver vaporization along the grain boundaries. Chen and Tuan [42] reported that the typical grain boundary diffusion length of silver in $BaTiO_3$ was 100–300 μm. This would account for the appearance of the "depletion" zone observed in the 0.3 mol% Ag samples. As the silver content increases more would become trapped along the grain boundaries causing the increase in the space charge effect and the dark gray discoloration. However, silver closer to the surface would be able to diffuse out of the pellet allowing the retention of the normal tan color.

The dielectric response for excess TiO_2 compositions, on the other hand, does show an influence by the presence of silver. First, there is a downward shift of T_c possibly resulting from the incorporation of silver into the perovskite crystal structure. Such a shift is a common occurrence for dopants [16] and generally arises from a decrease in the tetragonality of the unit cell, which is also observed for excess TiO_2.

Second, there was a decrease in K_{rm}, which is not correlated to the effects of grain size on the ferroelectric domains in $BaTiO_3$. Generally, the dielectric constant decreases as the

grain size increases due to the decreased intergranular stress (shown in Fig. 1.10). From this effect one would expect K_{rm} to increase. Of greater importance is the reduction in density observed with rising silver content. Because air has a very low dielectric constant (K~1) compared to $BaTiO_3$, an increase in the porosity would cause a significant drop in the dielectric constant. To test this idea, the empirical formula used to calculate the basic effect of a mixture of phases on the dielectric constant was utilized with the excess TiO_2 composition with no silver addition serving as a reference point [2]:

$$\ln K_m = \sum_i V_{fi} \ln K_i \qquad (5.6)$$

where K_m is the dielectric constant of the mixture, V_{fi} is the volume fraction of the i^{th} phase and K_i the dielectric constant of the i^{th} phase when it is 100% dense. From Figure 5.3 it can be seen that the measured data follows the same basic trend as the calculated values. The lower values for the measured data compared to the calculated is likely due to enclosed porosity which cannot be measured by the Archimedes method.

Finally, for excess TiO_2, there was a modest increase in tan δ possibly signifying the presence of charged defects. This could be the result from the increase in the space charge effect along with the likely tendency for Ag'_{Ba} to segregate to the grain boundaries.

$BaTiO_3$ compositions with excess BaO exhibit less of a dependence on the presence of silver. Similar to stoichiometric $BaTiO_3$, T_c remains constant. The space charge effect is also not as apparent, and in fact, tan δ_{rm} demonstrates a slight decrease. This suggests that silver is not as free to polarize compared to the other compositions. The reasons for this are unclear. It would be expected that Ag'''_{Ti} would have an incredibly low mobility due to the high lattice misfit and large associated charge. However, silver that did not dissolve into the

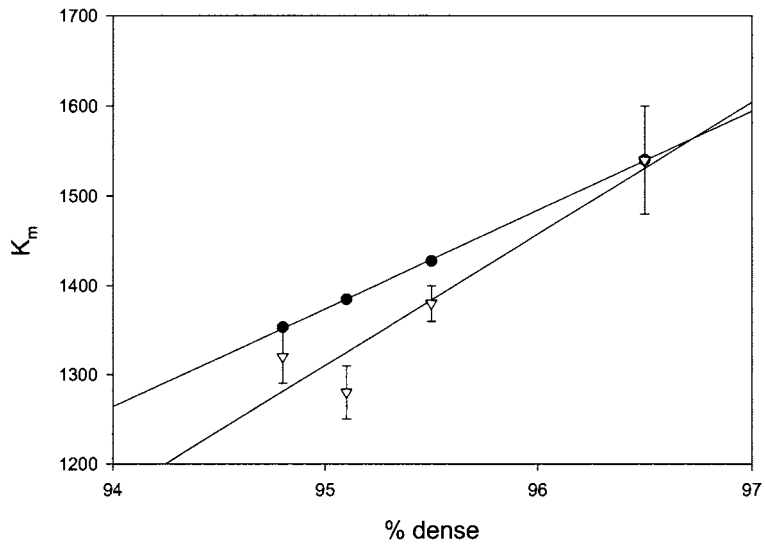

Figure 5.3: K_m as a function of percent density for $BaTiO_3$ + 0.5 mol% TiO_2 compositions where (▽) represents the measured values and (●) the calculated values

perovskite structure should be as mobile as that in the stoichiometric compositions. As the solubility of silver in excess BaO is very small, it is unlikely that enough silver has been incorporated into the bulk material to significantly deplete the amount of silver present in the grain boundaries.

On the other hand, there is a significant drop in K_{rm}. From the increase in tetragonality, it would be expected that K_{rm} would increase. A similar result would be predicted from the rise in density. However, the disappearance of the small abnormal grains would cause a decrease in K_{rm} due to the grain size effect. Because the size of the small grains was on the order of a few microns, their loss would have a profound consequence on the dielectric constant and is believed to be the primary cause of the reduction in K_{rm}.

For both the stoichiometric and excess TiO_2 compositions, at high silver concentrations (~ 0.3 mol% Ag) a strong dispersion in K was observed at high temperatures an example of which is shown in Figure 5.4. This is a strong indication of temperature activated space charge polarization. At these high silver concentrations, it is likely that the silver concentration at the grain boundary is significant. The excess BaO also exhibits some dispersion but not to the same degree.

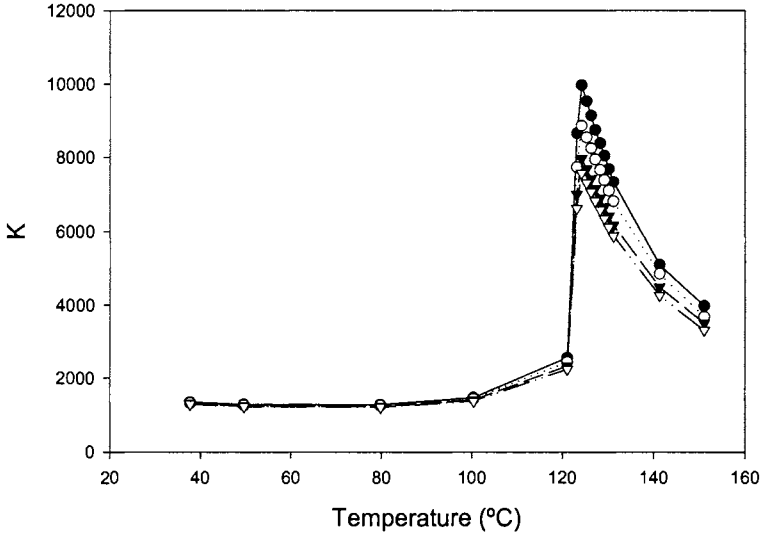

Figure 5.4: K as a function of temperature for $BaTiO_3$ + 0.3 mol% Ag; (●) 0.12 kHz, (○) 1 kHz, (▼) 10 kHz, (▽) 100 kHz

5.4 Conclusion

To summarize, the following conclusions can be made about the effects of silver additions on $BaTiO_3$:

1. The interaction of silver with $BaTiO_3$ is highly dependent on stoichiometry.
2. The solubility of silver in stoichiometric $BaTiO_3$ is negligible.

3. The solubility of silver in $BaTiO_3$ with excess TiO_2 or excess BaO is less than 0.06 mol% Ag.

4. Silver inhibits grain growth and suppresses the formation of large abnormal grains in $BaTiO_3$ with excess TiO_2.

5. Silver enhances grain growth and eliminates the formation of small abnormal grains and large porous cavities in $BaTiO_3$ with excess BaO.

6. The dielectric response of stoichiometric $BaTiO_3$ is not affected by silver except for an increase in the space charge effect.

7. Silver decreases T_c and K_{rm} and increases tan δ_{rm} and the space charge effect for $BaTiO_3$ with excess TiO_2.

8. Silver does not affect T_c but decreases K_{rm} and tan δ_{rm} for $BaTiO_3$ with excess BaO.

Future work in this area should include studies on grain growth kinetics especially for the excess BaO compositions. Also, because the assumed incorporation mechanisms for silver require compensation by oxygen vacancies, conductivity studies as a function of oxygen partial pressure would be enlightening. In the same vein, tests of the degradation resistance would provide valuable information as well, as oxygen vacancies are the primary cause of this phenomenon. Finally, diffusion studies of silver into $BaTiO_3$ are in order as research in this area is severally lacking.

APPENDIX A: DIELECTRIC TEMPERATURE SCANS

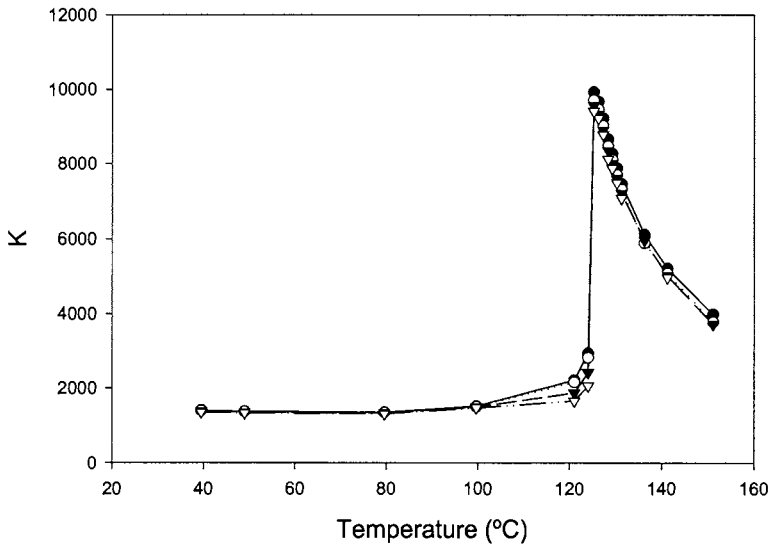

Figure A1: K as a function of temperature for $BaTiO_3$; (●) 0.12 kHz, (○) 1 kHz, (▼) 10 kHz, (▽) 100 kHz.

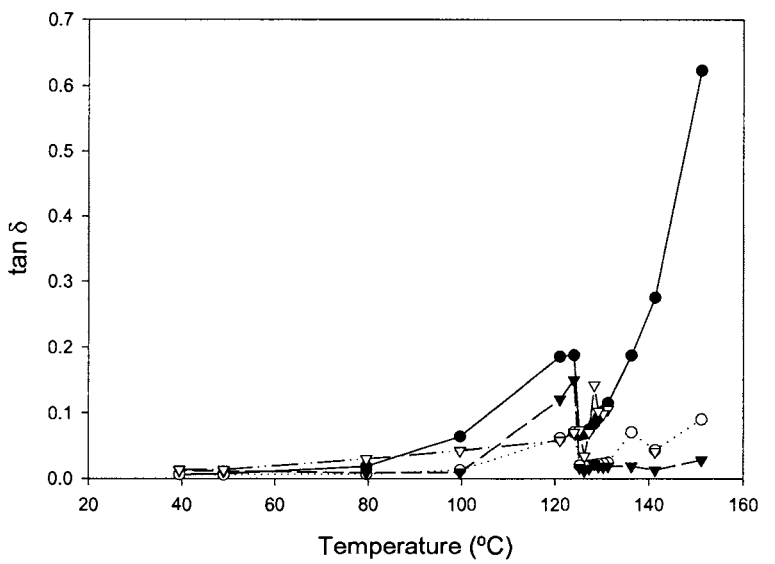

Figure A2: tan δ as a function of temperature for $BaTiO_3$; (●) 0.12 kHz, (○) 1 kHz, (▼) 10 kHz, (▽) 100 kHz.

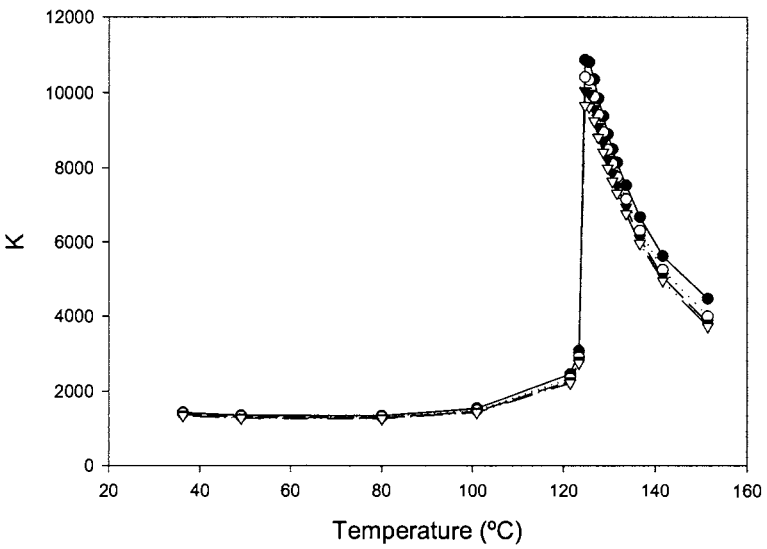

Figure A3: K as a function of temperature for $BaTiO_3$ + 0.06 mol% Ag; (●) 0.12 kHz, (○) 1 kHz, (▼) 10 kHz, (▽) 100 kHz.

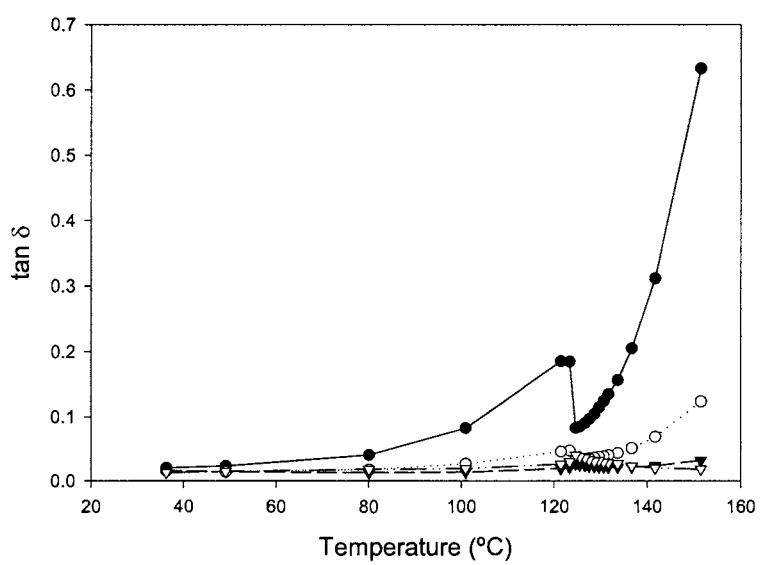

Figure A4: tan δ as a function of temperature for $BaTiO_3$ + 0.06 mol% Ag; (●) 0.12 kHz, (○) 1 kHz, (▼) 10 kHz, (▽) 100 kHz.

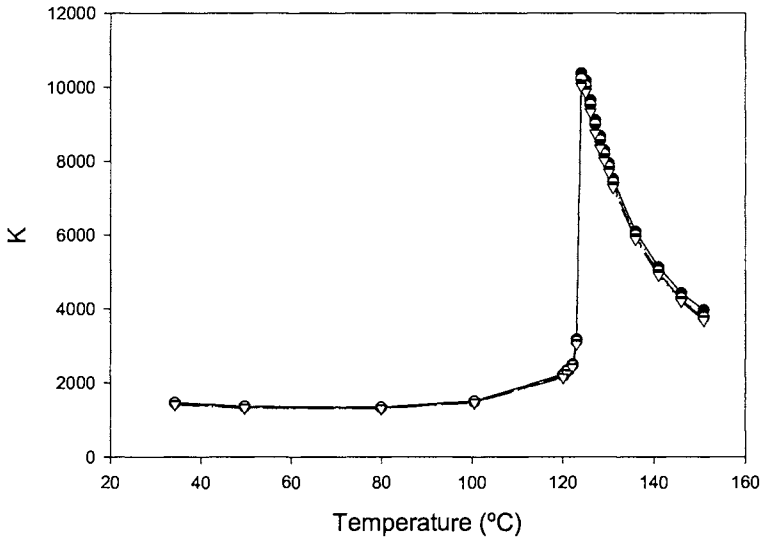

Figure A5: K as a function of temperature for $BaTiO_3$ + 0.1 mol% Ag; (●) 0.12 kHz, (○) 1 kHz, (▼) 10 kHz, (▽) 100 kHz

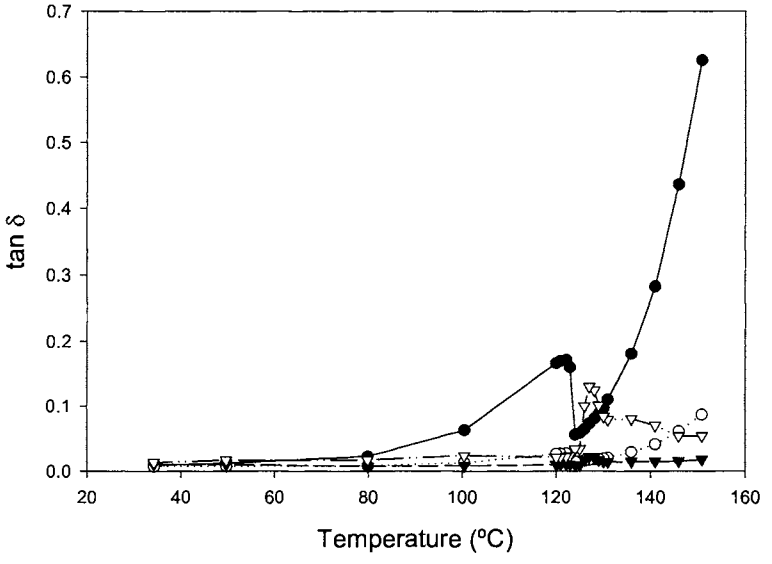

Figure A6: tan δ as a function of temperature for $BaTiO_3$ + 0.1 mol% Ag; (●) 0.12 kHz, (○) 1 kHz, (▼) 10 kHz, (▽) 100 kHz.

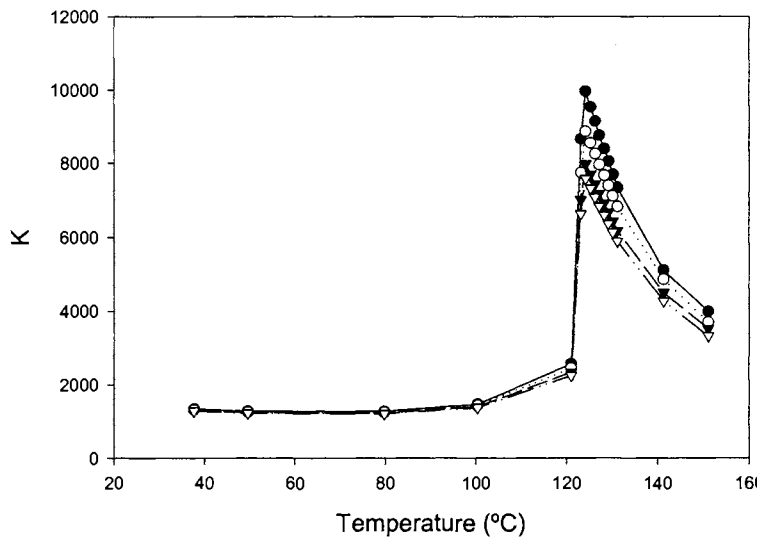

Figure A7: K as a function of temperature for $BaTiO_3$ + 0.3 mol% Ag; (●) 0.12 kHz, (○) 1 kHz, (▼) 10 kHz, (▽) 100 kHz

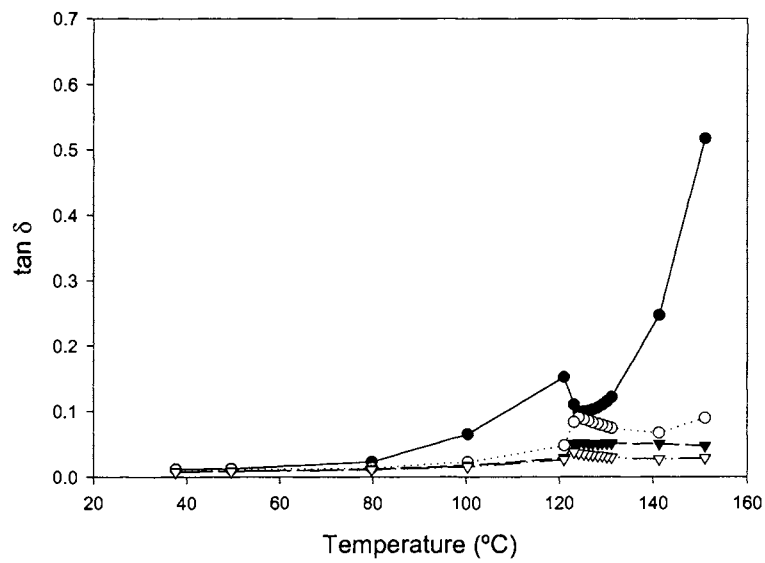

Figure A8: tan δ as a function of temperature for $BaTiO_3$ + 0.3 mol% Ag; (●) 0.12 kHz, (○) 1 kHz, (▼) 10 kHz, (▽) 100 kHz.

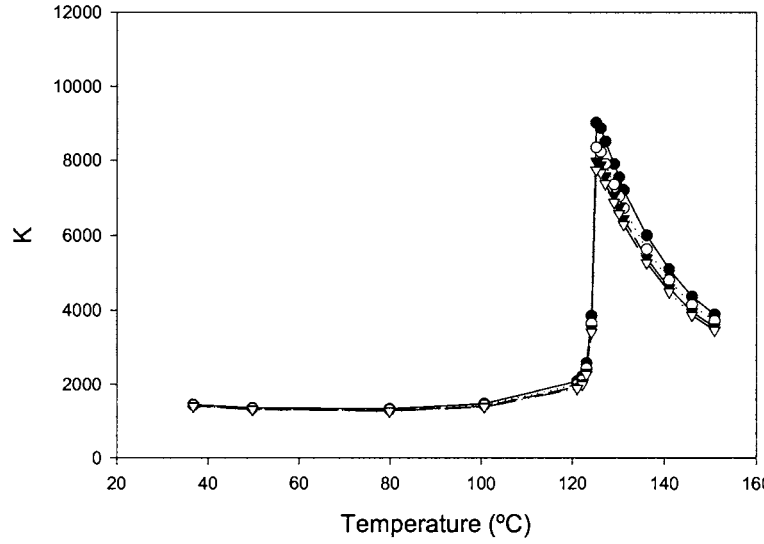

Figure A9: K as a function of temperature for $BaTiO_3$ + 0.5 mol% TiO_2; (●) 0.12 kHz, (○) 1 kHz, (▼) 10 kHz, (▽) 100 kHz

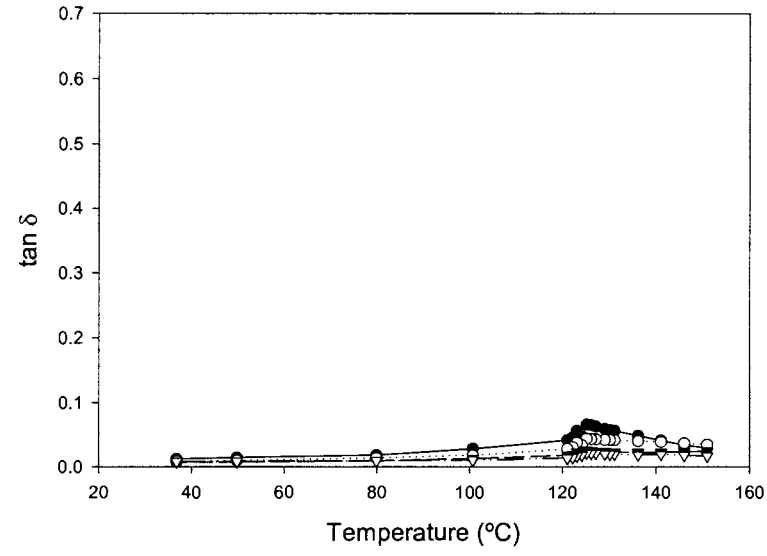

Figure A10: tan δ as a function of temperature for $BaTiO_3$ + 0.5 mol% TiO_2; (●) 0.12 kHz, (○) 1 kHz, (▼) 10 kHz, (▽) 100 kHz.

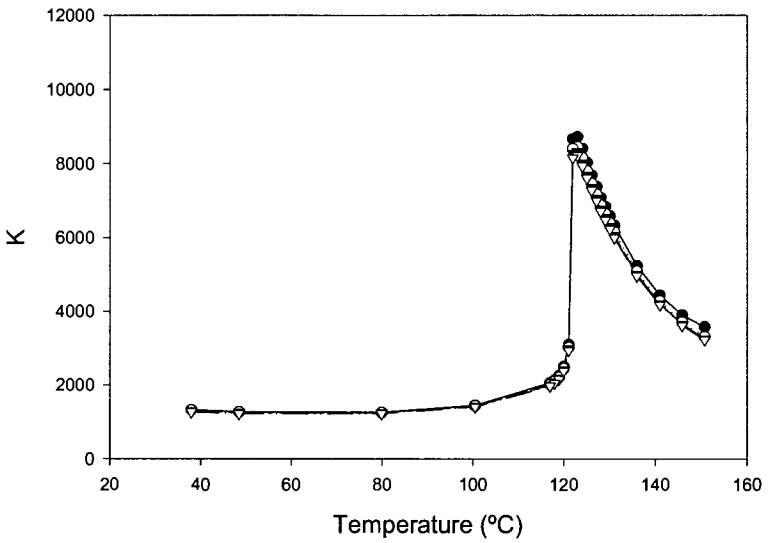

Figure A11: K as a function of temperature for $BaTiO_3$ + 0.5 mol% TiO_2 + 0.06 mol% Ag; (●) 0.12 kHz, (○) 1 kHz, (▼) 10 kHz, (▽) 100 kHz

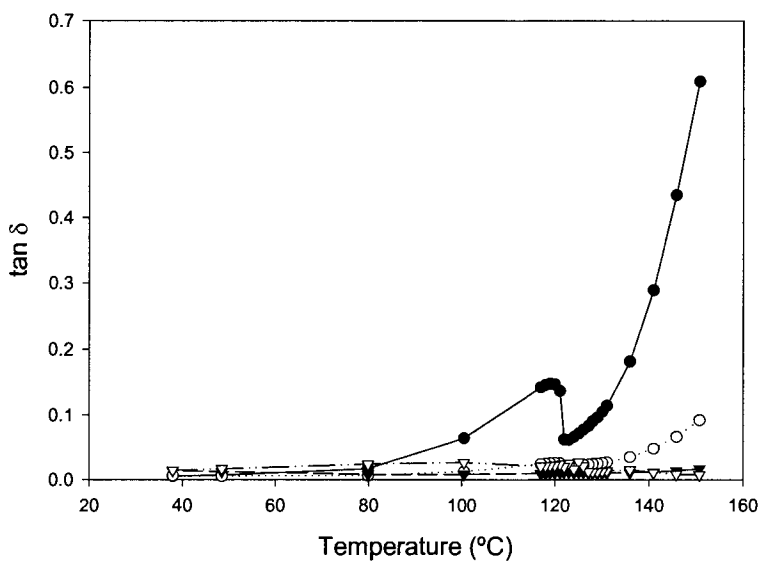

Figure A12: tan δ as a function of temperature for $BaTiO_3$ + 0.5 mol% TiO_2 + 0.06 mol% Ag; (●) 0.12 kHz, (○) 1 kHz, (▼) 10 kHz, (▽) 100 kHz.

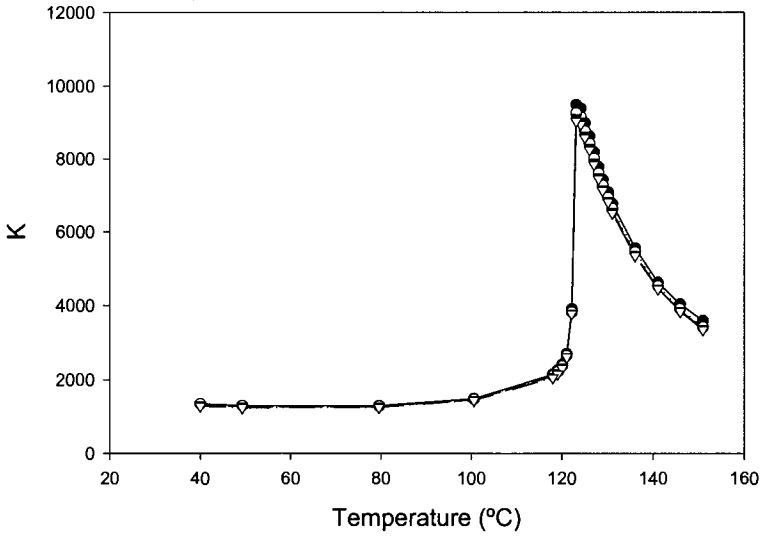

Figure A13: K as a function of temperature for $BaTiO_3$ + 0.5 mol% TiO_2 + 0.1 mol% Ag; (●) 0.12 kHz, (○) 1 kHz, (▼) 10 kHz, (▽) 100 kHz

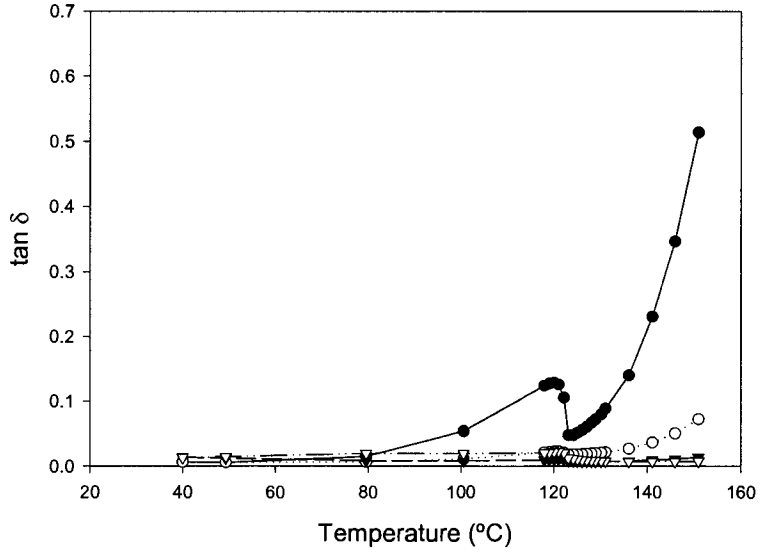

Figure A14: tan δ as a function of temperature for $BaTiO_3$ + 0.5 mol% TiO_2 + 0.1 mol% Ag; (●) 0.12 kHz, (○) 1 kHz, (▼) 10 kHz, (▽) 100 kHz.

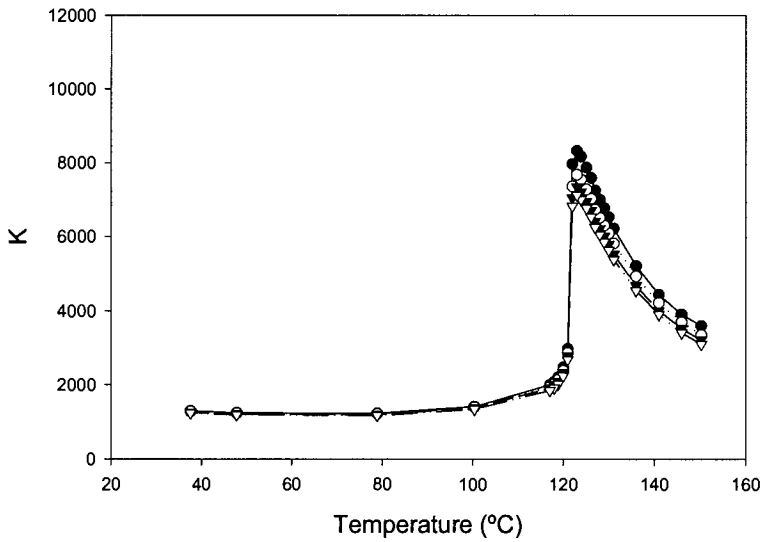

Figure A15: K as a function of temperature for $BaTiO_3$ + 0.5 mol% TiO_2 + 0.3 mol% Ag; (●) 0.12 kHz, (○) 1 kHz, (▼) 10 kHz, (▽) 100 kHz

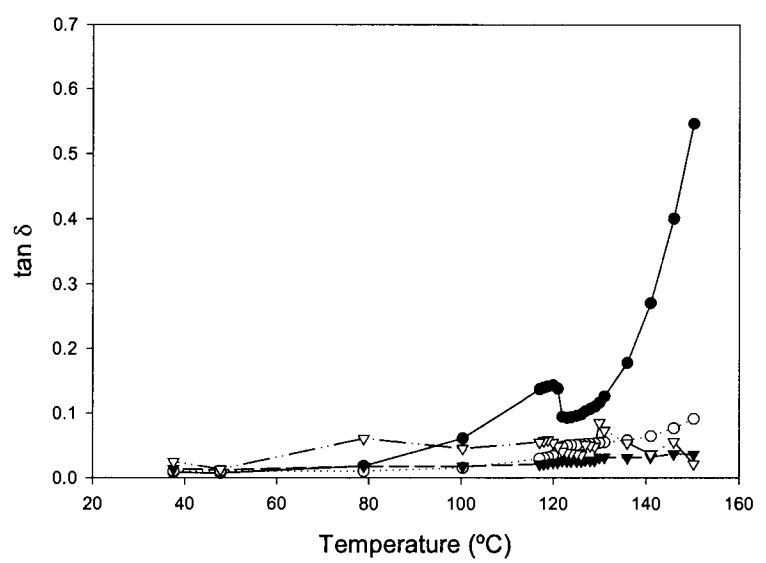

Figure A16: tan δ as a function of temperature for $BaTiO_3$ + 0.5 mol% TiO_2 + 0.3 mol% Ag; (●) 0.12 kHz, (○) 1 kHz, (▼) 10 kHz, (▽) 100 kHz.

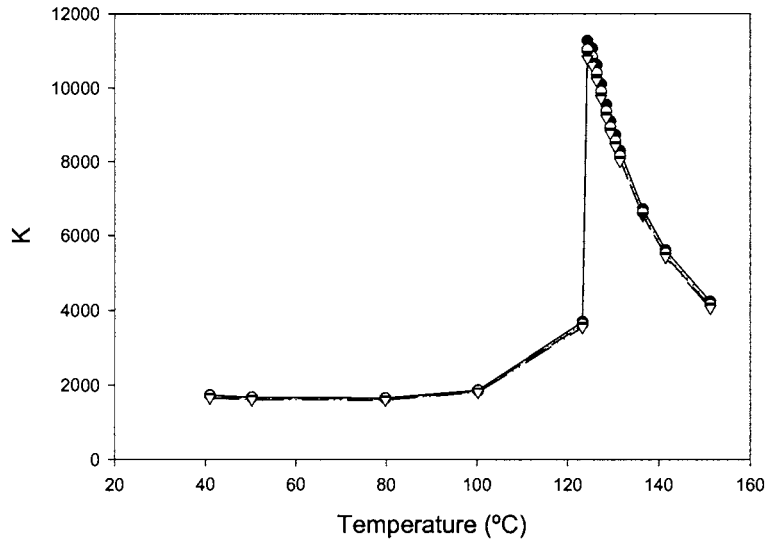

Figure A17: K as a function of temperature for $BaTiO_3$ + 0.5 mol% BaO; (●) 0.12 kHz, (○) 1 kHz, (▼) 10 kHz, (▽) 100 kHz

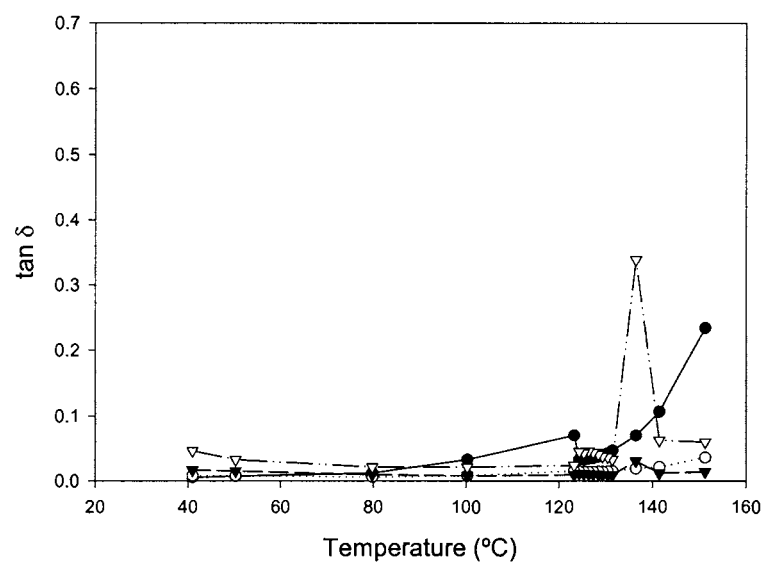

Figure A18: tan δ as a function of temperature for $BaTiO_3$ + 0.5 mol% BaO; (●) 0.12 kHz, (○) 1 kHz, (▼) 10 kHz, (▽) 100 kHz.

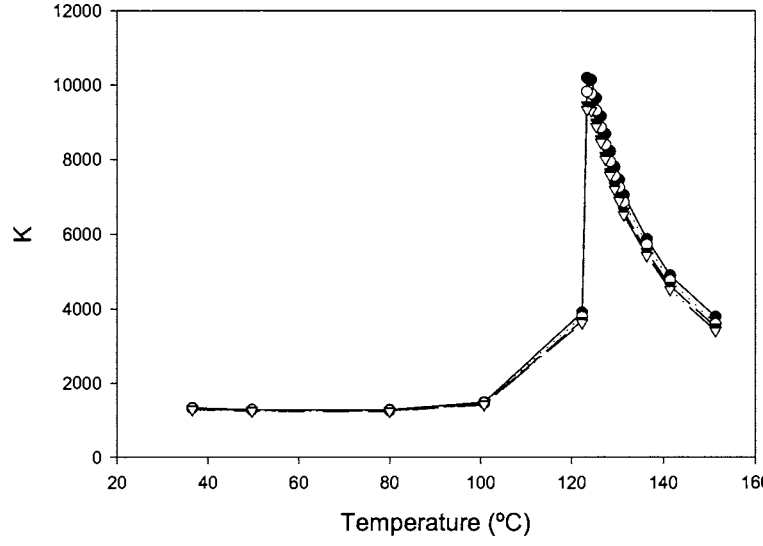

Figure A19: K as a function of temperature for $BaTiO_3$ + 0.5 mol% BaO + 0.06 mol% Ag; (●) 0.12 kHz, (○) 1 kHz, (▼) 10 kHz, (▽) 100 kHz

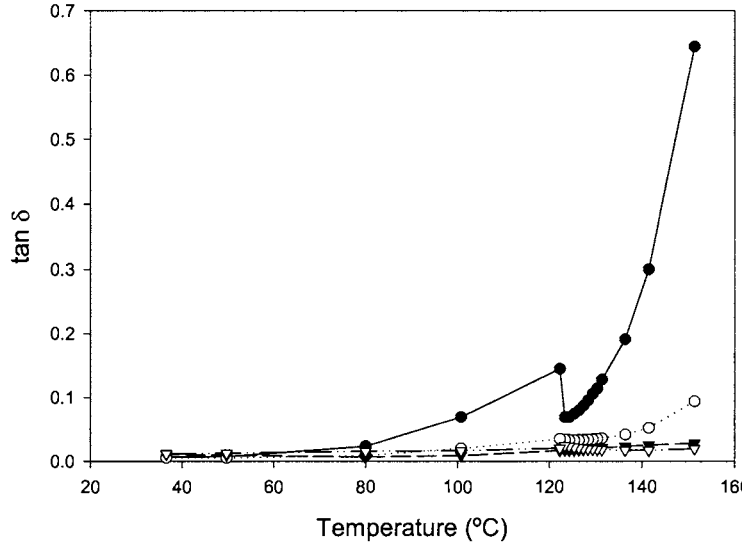

Figure A20: tan δ as a function of temperature for $BaTiO_3$ + 0.5 mol% BaO + 0.06 mol% Ag; (●) 0.12 kHz, (○) 1 kHz, (▼) 10 kHz, (▽) 100 kHz.

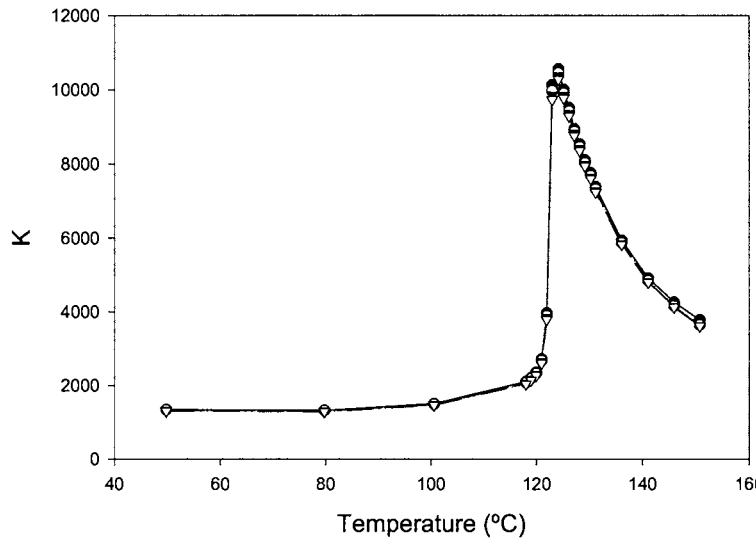

Figure A21: K as a function of temperature for $BaTiO_3$ + 0.5 mol% BaO + 0.1 mol% Ag; (●) 0.12 kHz, (○) 1 kHz, (▼) 10 kHz, (▽) 100 kHz

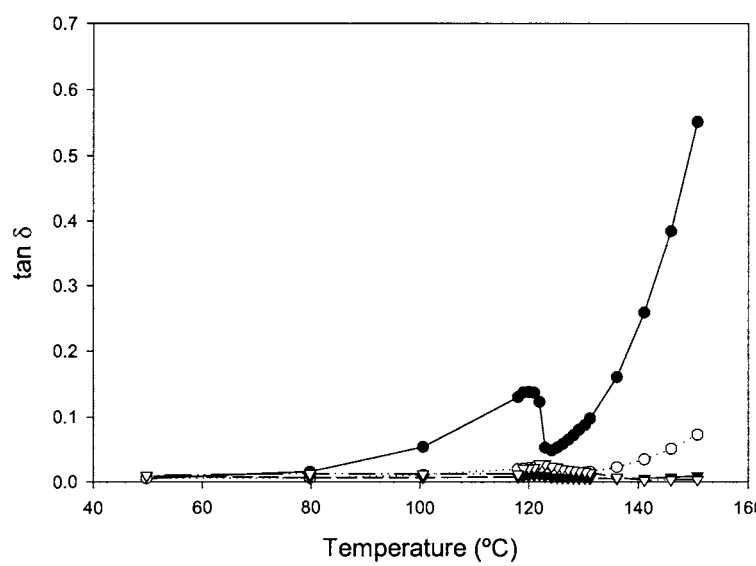

Figure A22: tan δ as a function of temperature for $BaTiO_3$ + 0.5 mol% BaO + 0.1 mol% Ag; (●) 0.12 kHz, (○) 1 kHz, (▼) 10 kHz, (▽) 100 kHz.

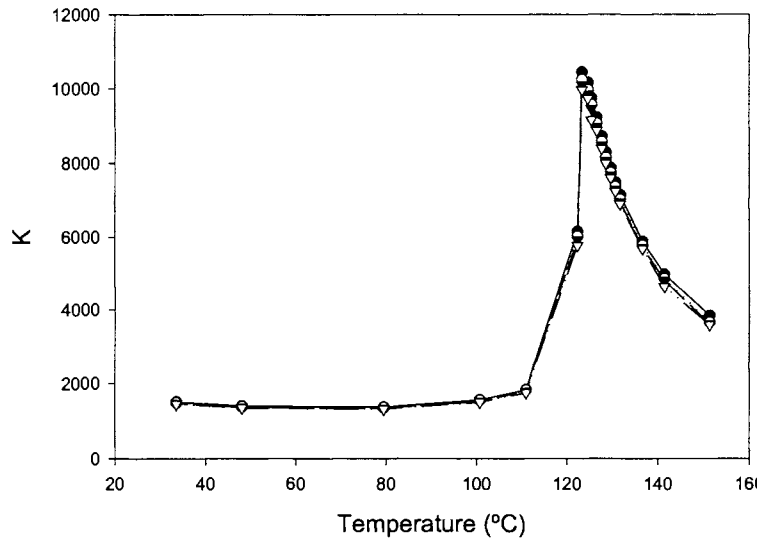

Figure A23: K as a function of temperature for $BaTiO_3$ + 0.5 mol% BaO + 0.3 mol% Ag; (●) 0.12 kHz, (○) 1 kHz, (▼) 10 kHz, (▽) 100 kHz

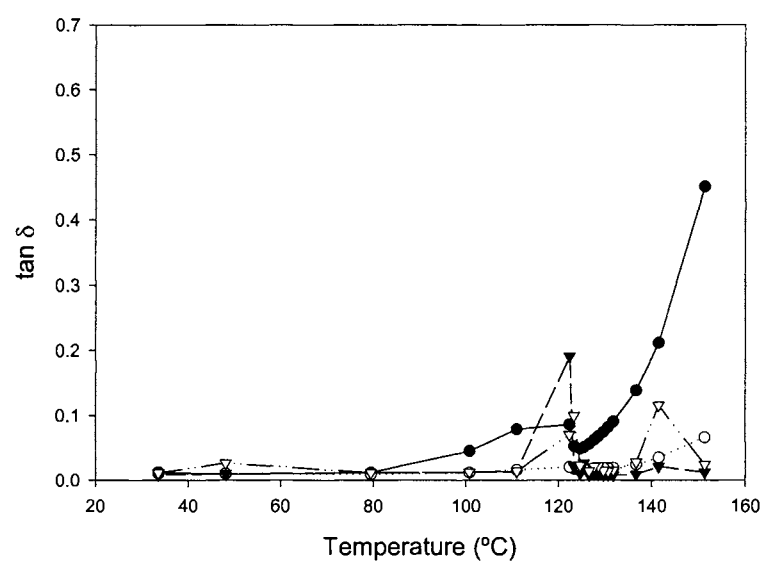

Figure A24: tan δ as a function of temperature for $BaTiO_3$ + 0.5 mol% BaO + 0.3 mol% Ag; (●) 0.12 kHz, (○) 1 kHz, (▼) 10 kHz, (▽) 100 kHz.

APPENDIX B: XRD SCANS

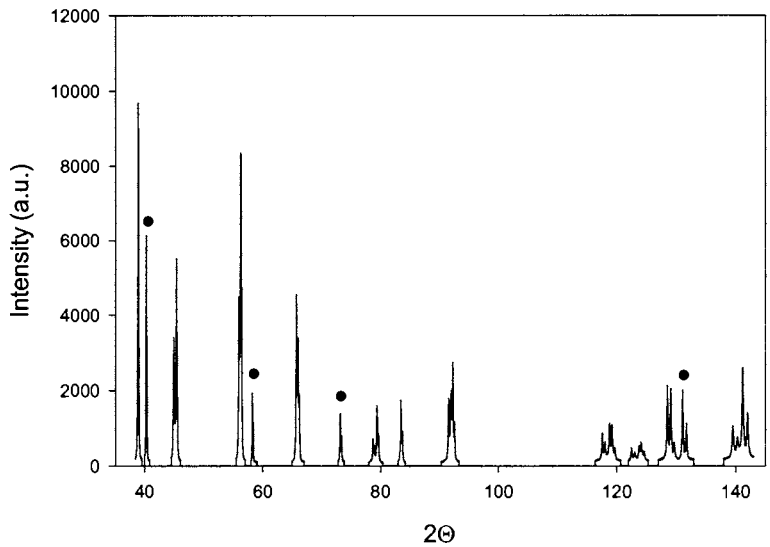

Figure B1: XRD scan of $BaTiO_3$. Tungsten peaks are indicated by (●).

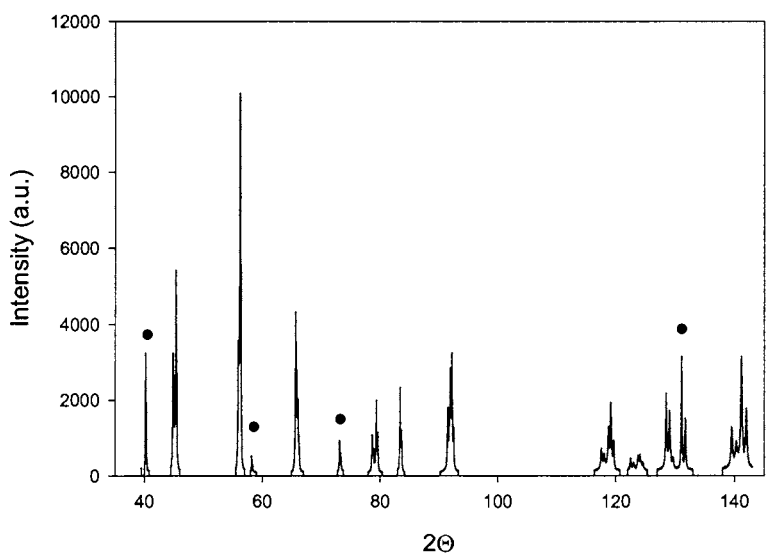

Figure B2: XRD scan of $BaTiO_3$ + 0.06 mol% Ag. Tungsten peaks are indicated by (●).

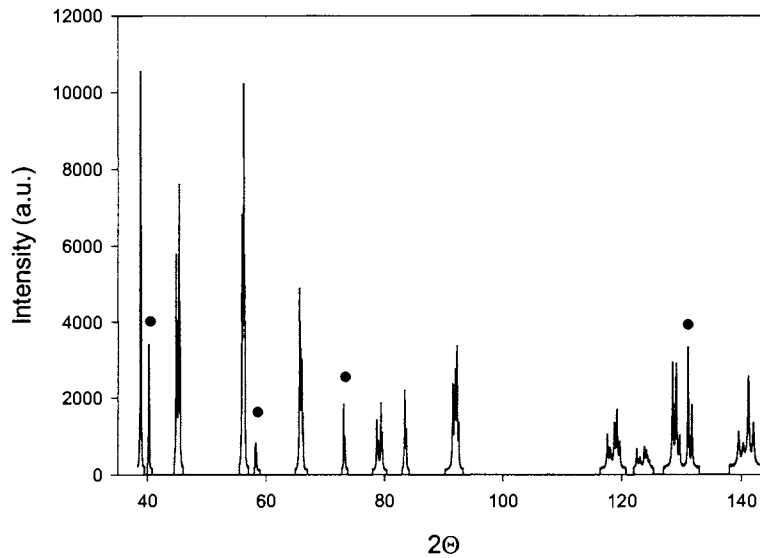

Figure B3: XRD scan of $BaTiO_3$ + 0.1 mol% Ag. Tungsten peaks are indicated by (●).

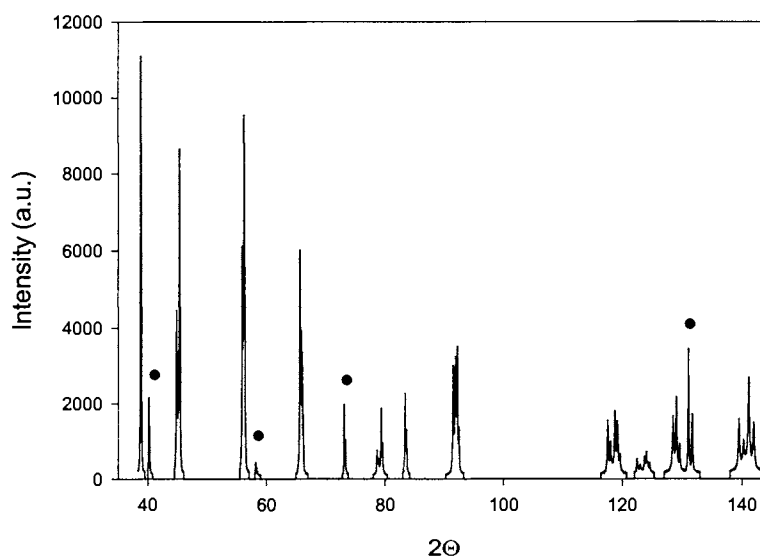

Figure B4: XRD scan of $BaTiO_3$ + 0.3 mol% Ag. Tungsten peaks are indicated by (●).

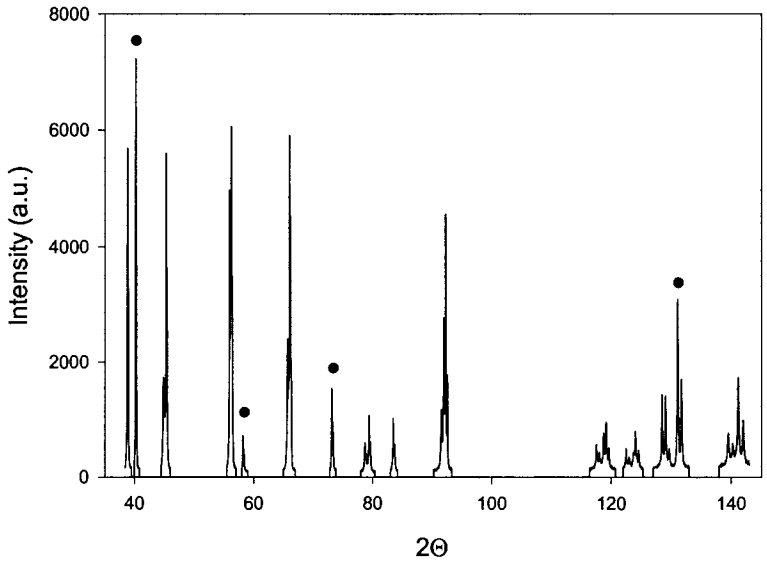

Figure B5: XRD scan of $BaTiO_3$ + 0.5 mol% TiO_2. Tungsten peaks are indicated by (●).

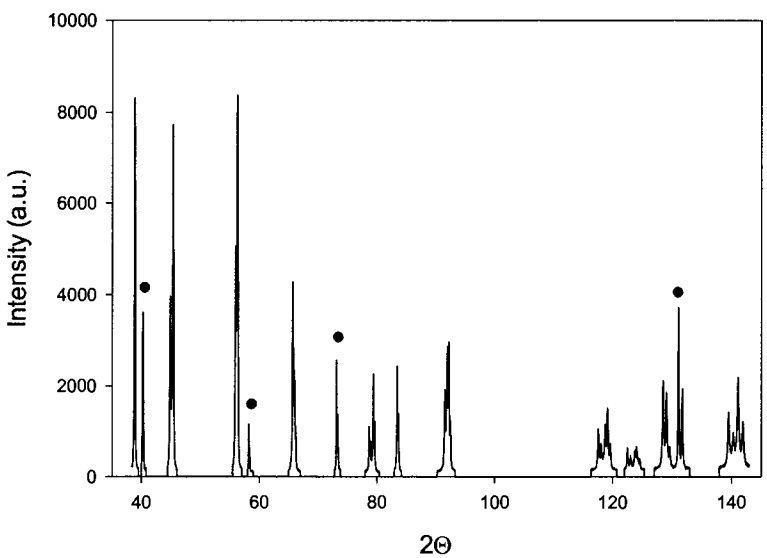

Figure B6: XRD scan of $BaTiO_3$ + 0.5 mol% TiO_2 + 0.06 mol% Ag. Tungsten peaks are indicated by (●).

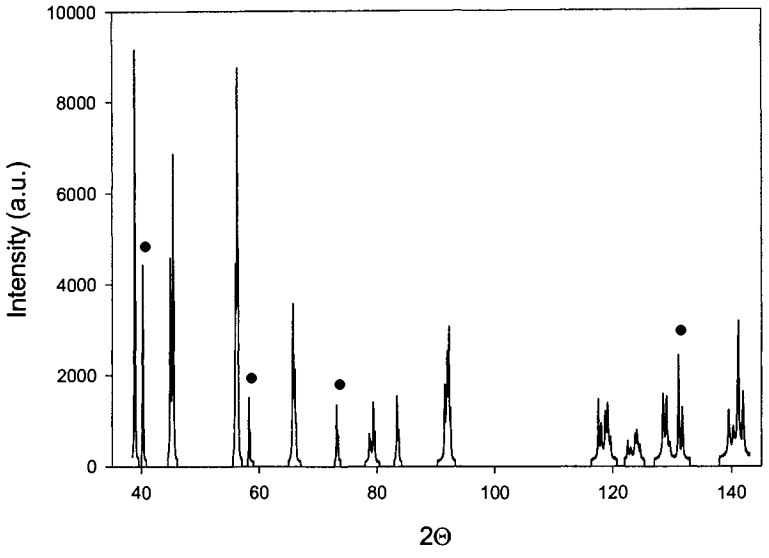

Figure B7: XRD scan of $BaTiO_3$ + 0.5 mol% TiO_2 + 0.1 mol% Ag. Tungsten peaks are indicated by (•).

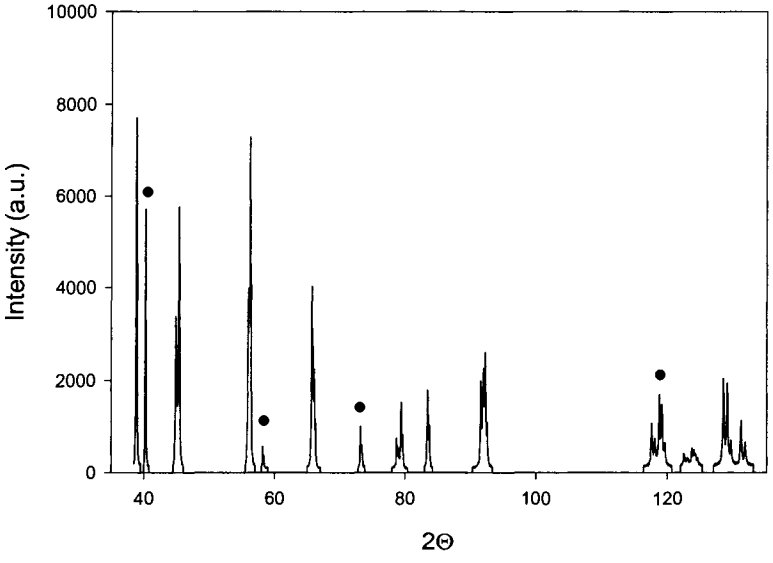

Figure B8: XRD scan of $BaTiO_3$ + 0.5 mol% TiO_2 + 0.3 mol% Ag. Tungsten peaks are indicated by (•).

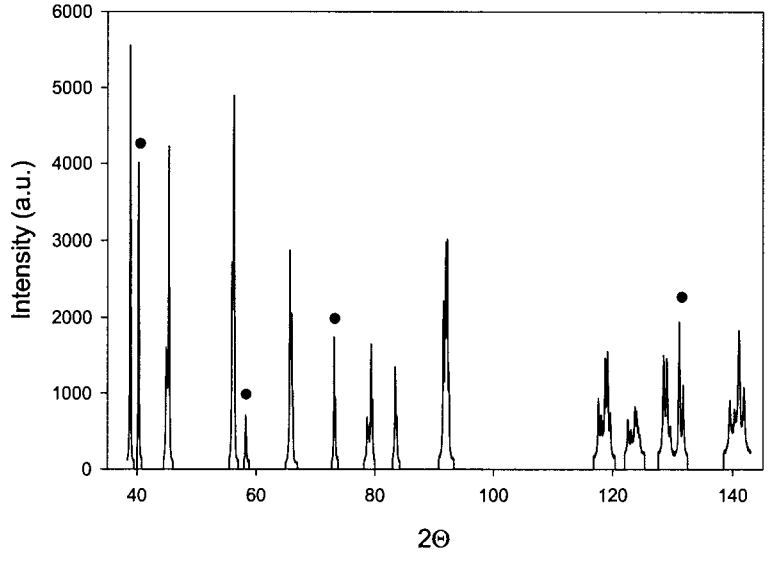

Figure B9: XRD scan of $BaTiO_3$ + 0.5 mol% BaO. Tungsten peaks are indicated by (●).

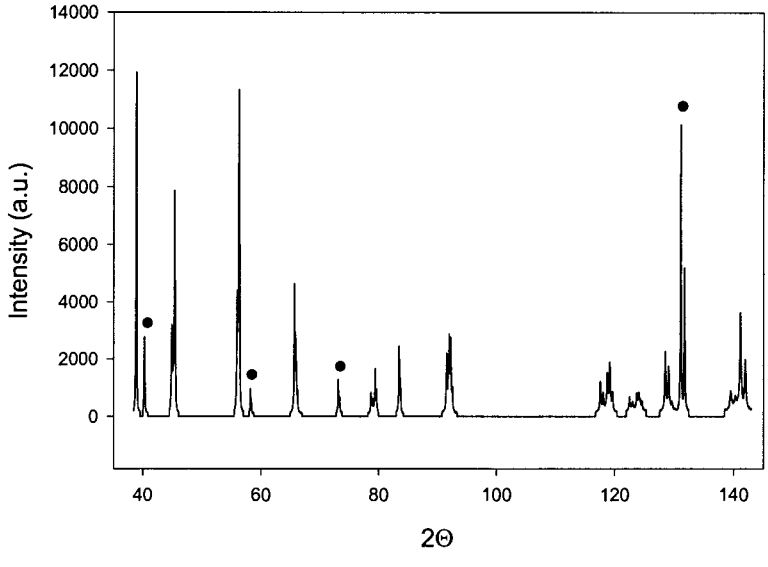

Figure B10: XRD scan of $BaTiO_3$ + 0.5 mol% BaO + 0.06 mol% Ag. Tungsten peaks are indicated by (●).

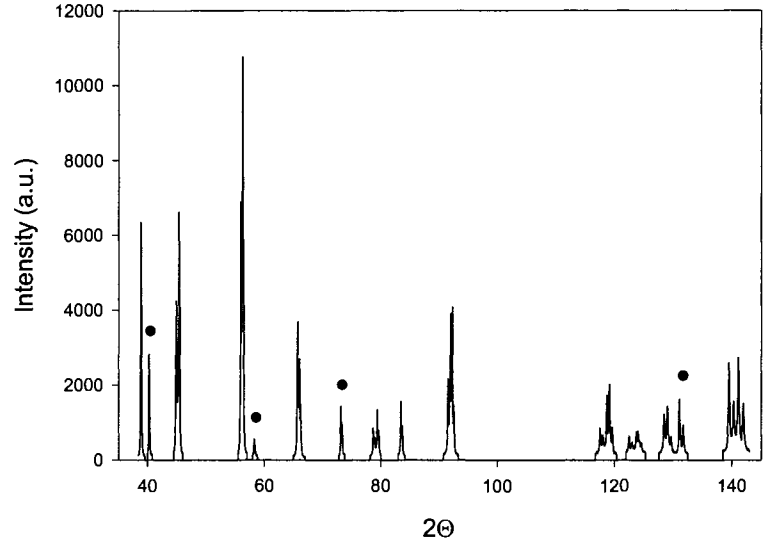

Figure B11: XRD scan of $BaTiO_3$ + 0.5 mol% BaO + 0.1 mol% Ag. Tungsten peaks are indicated by (●).

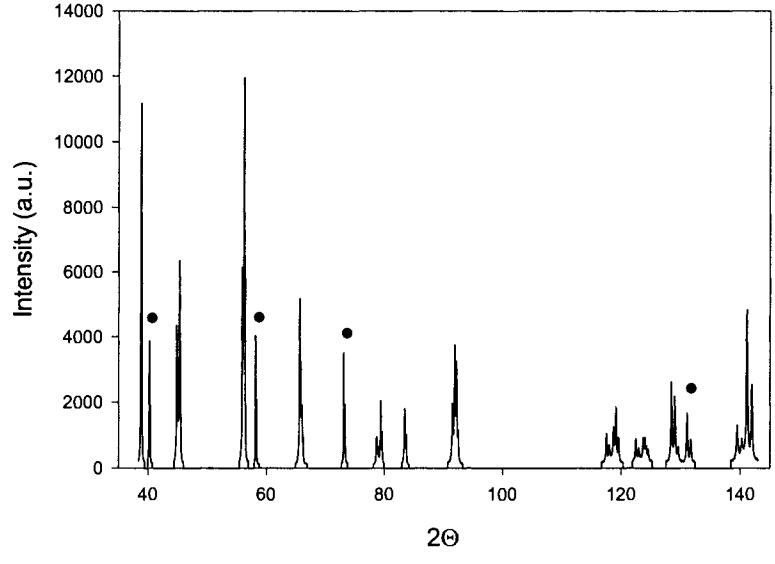

Figure B12: XRD scan of $BaTiO_3$ + 0.5 mol% BaO + 0.3 mol% Ag. Tungsten peaks are indicated by (●).

REFERENCES

1. Chu, Mike S. H. and Alan W. I. M. Rae, *Amer. Ceram. Soc. Bull.* **74** [6], p.69 (1995).
2. Moulson, A. J. and J. M. Herbert, *Electroceramics: Materials, Properties, Applications.* Chapman & Hall: New York, 1990.
3. Wang, Sea Fue and Joseph P. Dougherty, *J. Am. Ceram. Soc.* **77** [12], p.3051 (1994).
4. Sakabe, Yukio, *Ceramic Transactions: Multilayer Electronic Ceramic Devices, vol. 97.* Edited by Jau-Ho Jean *et al.* American Ceramic Society: Westerville, Ohio, 1999.
5. Adair, J. H. *et al.*, *J. Mater. Educ.* **9**, p. 75, (1987).
6. Morell, Antionette and Jean-Claude Niepce, *J. Mater. Educ.* **13**, p. 173, (1991).
7. Rase, D. E. and Rustum Roy, *J. Am. Ceram. Soc.* **38** [3], p.102 (1955).
8. Hwang, Jin Hyun and Young Ho Han, *Electrochemistry* **68** [6], p.423 (2000).
9. Chan, Helen M., Martin P. Harmer and Donald M. Smyth, *J. Am. Ceram. Soc.* **69** [6], p.507 (1986).
10. Xu, Yuhuan, *Ferroelectric Materials and Their Applications.* North-Holland: New York, 1991.
11. Flores-Ramirez, R. *et al.*, *Ferroelectrics.* **99**, p.195 (1989).
12. Rupprecht, G. and R. O. Bell, *Phys. Rev.* **135** [3A], p.A748 (1964).
13. Déri, Márta, *Ferroelectric Ceramics.* Gordon and Breach Science Publishers: New York, 1969.
14. Rustum, Roy, *J. Amer. Ceram. Soc.* **37** [12], p.581 (1954).
15. Park, J. G., T. S. Oh and Y. H. Kim, *J. Mater. Sci.* **27**, p.5713 (1992).
16. Buscaglia, M. T., *et al.*, *J. Eur. Ceram. Soc.* **20**, p1997 (2000).
17. Tsur, Yoed, *et al.*, *Jpn. J. Appl. Phys.* **40**, p. 225 (2001).
18. Hanafi, Z. M., S. A. A. Nasser and N. M. Molokkia, *Z. Phys. Chemie, Leipzig* **265** [6], p.1218 (1984).
19. Kishi, Hiroshi, *et al.*, *Jpn. J. Appl. Phys. Part 1* **38** [9B], p.5452 (1999).
20. Donohue, Jerry, Stanley J. Miller and Robert F. Cline, *Acta. Cryst.* **11**, p.693 (1958).
21. Han, Young Ho, John B. Appleby and Donald M. Smyth, *J. Amer. Ceram. Soc.* **70** [2], p.96 (1987).
22. Armstrong, Timothy R. and Relva C. Buchanan, *J. Am. Ceram. Soc.* **73** [5], p.1268 (1990).
23. Glinchuck, Maya D., *et al.*, *J. Mater. Chem.* **10** [4], p.941 (2000).
24. Bratschun, W. R., *J. Am. Ceram. Soc.* **45**, p.611 (1962).
25. Issa, M. A. A., *J. Mater. Sci.* **27** [13], p.3685 (1992).
26. Babu, A. Ramesh and A. V. Prasadarao, *J. Mater. Sci. Lett.* **16**, p.313 (1997).
27. Kowalski, K., *et al.*, *J. Phys. Chem. Solids* **62** [3], p.543 (2001).
28. Schmelz, H., *Phys. Status Solidi* **35** [1], p.219 (1969).
29. Shannon, R. D., *Acta Crystallogr.* **A32** [5], p.751 (1976).
30. Jia, Y. Q., *J. Solid State Chem.* **95**, p.184 (1991).
31. Randall, C. A. *et al.*, *J. Mater. Res.* **8** [4], p. 871 (1993).
32. Hennings, D. and G. Rosenstein, *J. Am. Ceram. Soc.* **67** [4], p. 249 (1984).

33. Hagemann, H. J., D. Hennings and R. Wernicke, *Philips Tech. Rev.* **41** [3], p.89 (1983/84).
34. Park, Yung and Yoonho Kim, *J. Mater. Res.* **10** [11], p.2770 (1995).
35. Chazono, Hirokazu and Masayuki Fujimoto, *Jpn. J. Appl. Phys. Part 1.* **34** [9B], p.5354 (1995).
36. Kim, Joo-Sun and Suk-Joong L. Kang, *J. Am. Ceram. Soc.* **82** [4], p.1085 (1999).
37. Azough, F., R. Al-Saffar and R. Freer, *J. Eur. Ceram. Soc.* **18** [7], p.751 (1998).
38. Rahaman, M. N., *Ceramic Processing and Sintering*. Marcel Dekker, Inc.: New York, 1995.
39. Frey, M. H., *et al.*, *Ferroelectrics* **206-207**, p.337 (1998).
40. Arlt, G., D. Hennings and G. de With, *J. Appl. Phys.* **58** [4], p.1619 (1985).
41. Massalski, Thaddeus B. ed., *Binary Alloy Phase Diagrams*. ASM International: Metals Park, Ohio, 1986.
42. Chen, Chin-Yi and Wei-Hsing Tuan. *J. Am. Ceram. Soc.* **83** [7], p.1693 (2000).
43. Chen, Chin-Yi and Wei-Hsing Tuan. *J. Am. Ceram. Soc.* **83** [12], p.2988 (2000).
44. Villegas, M. *et al.*, *J. Mater. Sci.* **29** [19], p.4999 (1994).
45. Slinkina, M. V. *et al*, *Inorg. Mater.* **26** [12], p. 2266 (1990).
46. Slinkina, M. V., G. I. Dontsov and V. M. Zhukovsky, *J. Mater. Sci.* **28** [19], p.5189 (1993).
47. Caballero, C. *et al*, *J. Mater. Sci.* **32**, p.3257 (1997).
48. Kulikov, G. S. *et al*, *Ferroelectrics* **144**, p.61 (1993).
49. Zuo, Ruzhong, Longtu Li and Zhilun Gui, *Ceram. Int.* **26**, p.673 (2000).
50. Zuo, Ruzhong, *et al, Br. Ceram. Trans.* **100** [1], p.38 (2001).
51. Maher, Galeb H., *J. Am. Ceram. Soc.* **66** [6], p.408 (1983).
52. Ikushima, Hiroshi and Shigeru Hayakawa. *Japan. J. Appl. Phys.* **4** [5], p.328 (1965).
53. Halder, N. *et al.*, *Mater. Res. Bul.* **34** [4], p.545 (1999).
54. Smyth, D. M. *The Defect Chemistry of Metal Oxides*. Oxford University Press: New York, 2000.
55. Nowotny, Janusz and Mieczyslaw Rekas, *Solid State Ionics* **49**, p.135 (1991).
56. Schmelz, H, *Powder Metall. Int.* **7** [1], p.176 (1975).
57. Smyth, Donald M., Martin P. Harmer and Ping Peng, *J. Am. Ceram. Soc.* **72** [12], p.2276 (1989).
58. Tsai, M.S. and T.Y. Tseng, *Mater. Chem. Phys.* **57**, p.47 (1998).
59. Yoo, Han-Ill and Chang-Rock Song, *Solid State Ionics* **135**, p.619 (2000).
60. Nowotny, Janusz and Mieczyslaw Rekas, *Ceram. Int.* **20** (1994).
61. Aggarwal, Sanjeev and R. Ramesh, *Annu. Rev. Mater. Sci.* **28**, p.463 (1998).
62. Lewis, G. V., C. R. A. Catlow and R. E. W. Casselton, *J. Am. Ceram. Soc.* **68** [10], p.555 (1985).
63. Sato, Shigeki, *et al.*, *Jpn. J. Appl. Phys. Part 1* **36** [9B], p.6016 (1997).
64. Zhang, Xiao Wen, *et al.*, *J. Am. Ceram. Soc.* **70** [2], p.100 (1987).
65. Cullity, B. D., *Elements of X-Ray Diffraction*. Addison-Wesley Publishing Company: Reading, Massachusetts, 1978.
66. Roisnel, T. and J. Rodríguez-Carvajal, International Union of Crystallography: Commission for Powder Diffraction Newsletter, No. 20 (May-August) Summer 1998.

67. ASTM Designation E 112-88, 1996 Annual Book of ASTM Standards, Vol. 3.01. American Society of Testing and Materials: Philadelphia, PA, 1996.
68. Mendelson, Mel I., *J. Am. Ceram. Soc.* **52** [8], p.443 (1969).
69. Samara, G. A., *Phys. Rev.* **151** [2] (1966) p.378.
70. Kulcsar, Frank, *J. Am. Ceram. Soc.* **39** [1], p.13 (1956).
71. Sharma, R. K., N. H. Chan and D. M. Smyth, *J. Am. Ceram. Soc.* **64** [8], p.448 (1981).
72. Lin, Ming-Hong, Jung-Fang Chou and Hong-Yang Lu, *J. Euro. Ceram. Soc.* **20**, p.517 (2000).
73. Lin, Ming-Hong, Jung-Fang Chou and Hong-Yang Lu, *J. Am. Ceram. Soc.* **83** [9], p.2155 (2000).
74. Hu, Y. H., M. P. Harmer and D. M. Smyth, *J. Am. Ceram. Soc.* **68** [7], p.372 (1985).
75. Čeh, M. and D. Kolar, *Mat. Res. Bull.* **29** [3], p.269 (1994).
76. Rahaman, M. N., *Ceramic Transactions: Dielectric Ceramic Materials, vol. 100.* Edited by K.M. Nair, A.S. Bhalla. American Ceramic Society: Westerville, Ohio, 1999.
77. Cahn, J. W., *Acta Metall.* **10** [9], p.789 (1962).
78. Chiang, Yet-Ming and Touichi Takagi, *J. Am. Ceram. Soc.* **73** [11], p.3278 (1990).
79. Desu, Seshu B. and David A. Payne, *J. Am. Ceram. Soc.* **73** [11], p.3398 (1990).

AKNOWLEDGEMENTS

Nothing is accomplished without the aid of others, be it the gift of inspiration, guidance or the simple belief that you can accomplish what you have set out to do. This page is dedicated to all those who have helped me throughout my master's research and college career. To start, I would like to thank my major professor, David Cann, without whom this project would not have been possible. Thank you for listening to my views and pointing out ideas that I had not yet considered. I would also like to thank my other major professor, Brian Gleeson, for being an outstanding resource. Our discussions helped clarify my understanding of metal-ceramic diffusion. I am also grateful to my final committee member, Dennis Johnson, for his advice and insight.

Further thanks are in order for my fellow labmate, Julie Kidd, who performed all the SEM work for this project, freeing me to concentrate on other things. You did an excellent job. I would also like to show my appreciation to my other labmates, Bruce Gall, Megean Marquardt, Jane Clayton, Charles Chao and Nathan Ashmore for their assistance in my work and also helping me to relax. Thank your for choosing *Moonboots* as the "official" lab song and for introducing me to a number of sports I am terrible at, including golf and sand volleyball, although I think I am improving at pool.

I would like to extend my gratitude to my friends and the MSE administrative staff who were always there when I needed them and willing to taste whatever new cooking experiment I was trying. Thank you for the smiles, encouragement and the many sandwiches ordered at Jimmy Johns. Finally, I would like to thank my family, especially my parents, who always believed in me. I could not have done this without you.